



# MIT Open Access Articles

## *Formation and composition of the Late Cretaceous Gangdese arc lower crust in southern Tibet*

The MIT Faculty has made this article openly available. **Please share** how this access benefits you. Your story matters.

<b>Citation</b>	Guo, Liang et al. "Formation and composition of the Late Cretaceous Gangdese arc lower crust in southern Tibet." Contributions to Mineralogy and Petrology 175, 6 (June 2020): 58 © 2020 Springer-Verlag GmbH Germany, part of Springer Nature
<b>As Published</b>	<a href="https://doi.org/10.1007/s00410-020-01696-y">https://doi.org/10.1007/s00410-020-01696-y</a>
<b>Publisher</b>	Springer Science and Business Media LLC
<b>Version</b>	Author's final manuscript
<b>Citable link</b>	<a href="https://hdl.handle.net/1721.1/128904">https://hdl.handle.net/1721.1/128904</a>
<b>Terms of Use</b>	Creative Commons Attribution-Noncommercial-Share Alike
<b>Detailed Terms</b>	<a href="http://creativecommons.org/licenses/by-nc-sa/4.0/">http://creativecommons.org/licenses/by-nc-sa/4.0/</a>

## Formation and composition of the Late Cretaceous Gangdese arc lower crust in southern Tibet

**Cite this article as:** Liang Guo, Oliver Jagoutz, William J. Shinevar and Hong-Fei Zhang, Formation and composition of the Late Cretaceous Gangdese arc lower crust in southern Tibet, Contributions to Mineralogy and Petrology <https://doi.org/10.1007/s00410-020-01696-y>

This Author Accepted Manuscript is a PDF file of an unedited peer-reviewed manuscript that has been accepted for publication but has not been copyedited or corrected. The official version of record that is published in the journal is kept up to date and so may therefore differ from this version.

Terms of use and reuse: academic research for non-commercial purposes, see here for full terms. <https://www.springer.com/aam-terms-v1>

Author accepted manuscript

**Formation and composition of the Late Cretaceous Gangdese arc lower crust in southern****Tibet**

Liang Guo<sup>1,2\*</sup>, Oliver Jagoutz<sup>2</sup>, William J. Shinevar<sup>3</sup>, Hong-Fei Zhang<sup>1</sup>

<sup>1</sup> State Key Laboratory of Geological Processes and Mineral Resources and School of Earth Sciences, China

University of Geosciences, Wuhan 430074, People's Republic of China

<sup>2</sup> Department of Earth, Planetary and Atmospheric Sciences, Massachusetts Institute of Technology, 77

Massachusetts Avenue, Cambridge, MD 02139, USA

<sup>3</sup> Massachusetts Institute of Technology/Woods Hole Oceanographic Institution Joint Program in

Oceanography/Applied Ocean Science and Engineering, Woods Hole, MA 02543, USA

\*Corresponding author: Liang Guo (E-mail: lguo@cug.edu.cn)

**Abstract**

Arc lower crust plays a critical role in processing mantle-derived basaltic melts into the intermediate continental crust, yet can only be studied indirectly or in exposed arc sections. Compared with the relatively well-studied oceanic arc sections (e.g., Kohistan and Talcetna), the composition and formation mechanisms of continental arc lower crust remain less clear. Here we present a geochronological and geochemical study on the Lilong Complex and the Wolong granitoids from the Gangdese arc deep crustal section in southern Tibet. The Lilong Complex is composed of the early (85–95 Ma) mafic-intermediate sequence and late (85–86 Ma) ultramafic sequence. The Lilong crustal section exposed crustal depth extending from ~42–17 km based on the geobarometry. The mafic-intermediate sequence is a damp (low H<sub>2</sub>O) igneous differentiation sequence characterized by the subsequent appearance of pyroxene → plagioclase → amphibole → biotite. The ultramafic sequence represents a wet igneous differentiation sequence composed of olivine → pyroxene → amphibole → plagioclase. The 74–84 Ma Wolong granitoids were formed by fractional crystallization of wet magma and intra-crustal assimilation. Calculated seismic properties of the Gangdese deep arc crust are comparable to the average continental crust at similar depth. The average composition of the Gangdese arc lower crust is basaltic andesite with SiO<sub>2</sub> of ~54 wt%. The highly incompatible elements in the Gangdese arc lower crust are systematically higher than those of the oceanic arc and are comparable with the estimates of lower continental crust, suggesting continental arc magmatism significantly contributes to the formation of continental crust.

**Keywords:** Gangdese arc; lower crust; fractional crystallization; trace element; continental crust

## Introduction

Arc magmatism is regarded to be the main mechanism responsible for generating andesitic continental crust (Taylor and McLennan 1995). As most primitive arc melts are basaltic in composition (Schmidt and Jagoutz 2017), these melts are thought to differentiate into a dense cumulate/residue and a complementary felsic melt. It is also hypothesized that the bulk arc crust becomes andesitic in composition following delamination of the dense mafic component (Arndt and Goldstein 1989; Jagoutz and Kelemen 2015; Kay and Kay 1993). This scenario has been supported by the chemical differentiation of Kohistan and Talkeetna oceanic arcs (Jagoutz and Behn 2013). Although major element bulk compositions of the density-sorted oceanic arc crust are compatible with the bulk continental crust, oceanic arc lower crust is significantly depleted in highly incompatible elements (Jagoutz and Kelemen 2015; Jagoutz and Schmidt 2012) compared with the estimates of lower continental crust (LCC) (Hacker et al. 2015; Jagoutz et al. 2011; Kelemen and Behn 2016). As an alternative to the magmatic differentiation coupled with delamination mechanism, it has been proposed that the relamination of felsic materials at the base of the crust is a crucial mechanism to form intermediate continental crust composition (Hacker et al. 2011, 2015; Kelemen and Behn 2016).

Although numerous studies have been carried out on the xenoliths from the continental arc lower crust in the Sierra Nevada (e.g., Ducea and Saleeby 1998; Lee et al. 2006) or exposures of paleo-continental arc sections in the southern Sierra Nevada, the Fiordland in New Zealand, the Gangdese arc in South Tibet or the Famatinian in NW Argentina (Chapman et al. 2012; Otamendi et al. 2012; Stowell et al. 2014; Walker et al. 2015; Xu et al. 2019), the construction processes and composition of continental arc lower crust are still poorly constrained. For example, the importance of partial melting of preexisting crust (Ducea and Saleeby 1998; Otamendi et al. 2012; Stowell et al. 2014) versus crystallization-differentiation of arc magma (Jagoutz and Klein 2018; Lee et al. 2006; Walker et al. 2015) as the main differentiation mechanism remains debated and probably vary from arc to arc. It is also

unclear whether the trace element composition of continental arc lower crust is similar to the oceanic arcs lower crust or the LCC. Accordingly, insight into the formation mechanisms and composition of **continental** arc lower crust is critical **to understand continental crust formation**.

The recently discovered Lilong Gangdese arc lower crustal section (Guo et al. 2012; Zhang et al. 2020) is a continuous **exposure** of a continental arc lower crust (Fig. 1) ranging in depth from ~42–17 km. Here, we present U–Pb zircon geochronology, whole-rock major and trace elements, as well as Sr–Nd–Hf isotope data to understand the construction mechanism and **composition** of the Gangdese arc lower crust. **We show** the entire Lilong deep crustal section was built dominantly through early (85–95 Ma) damp and late (74–86 Ma) wet fractional crystallization of arc magmas. **In addition, the** calculated seismic properties and geochemical composition of the Gangdese arc lower crust **agree well with estimates** of the LCC. **Therefore, we** propose that the continental arc magmatism **plays a vital role in making** the continental crust.

### **Geological setting**

**The Gangdese arc is located in the Lhasa terrane in the southern Tibet (Fig. 1A). The Lhasa terrane is separated from the Qiangtang terrane to the north by the Bangong–Nujiang suture zone and from the Indian Plate to the south by the Indus–Yarlung Tsangpo suture zone (Fig. 1A). The Lhasa terrane is subdivided into southern, central, and northern Lhasa subterrane (Fig. 1A) by the Luobadui–Milashan fault and the Shiquanhe–Nam Tso Mélange zone (Zhu et al. 2011). The central Lhasa subterrane is underlain by Precambrian crystalline basement and is covered by Permo–Carboniferous metasedimentary rocks and Late Jurassic–Early Cretaceous volcano-sedimentary rocks (Pan et al. 2006; Zhu et al. 2011). Abundant Mesozoic–Cenozoic plutonic rocks intruded the Carboniferous–Cretaceous volcano-sedimentary rocks (Zhu et al. 2011). The northern Lhasa subterrane is mainly composed of Jurassic–Cretaceous volcano-sedimentary sequence with minor Triassic sedimentary rocks with Mesozoic plutonic**

rocks in its western and eastern parts (Zhu et al. 2011). The southern Lhasa subterrane is dominated by the Mesozoic-Cenozoic Gangdese batholith and the associated Linzizong volcanic succession, with minor Triassic-Cretaceous volcano-sedimentary rocks (Ji et al. 2009; Pan et al. 2006). A few Cambrian and Late Devonian-Early Carboniferous plutons have been reported in the eastern part of the southern Lhasa subterrane (Dong et al. 2010b; Guo et al. 2017; Ji et al. 2012). The Lhasa terrane collided with the Qiangtang terrane in the Early Cretaceous, which resulted in strongly S-N crustal shortening of the central-northern Lhasa subterrane (Kapp et al. 2007; Murphy et al. 1997). During the Mesozoic and early Cenozoic, northward subduction of the Neo-Tethyan oceanic slab underneath the southern margin of the Lhasa terrane led to the emplacement of voluminous Gangdese batholith into the Lhasa terrane basement as well as the eruption of the volcanic rocks (Yin and Harrison 2000). Geochronological studies reveal that the Gangdese arc magmatism started in the Triassic and persisted till the Paleocene with three magmatic flare-up events at 200–160 Ma, 120–105 Ma and 100–80 Ma (Ji et al. 2009; Ma et al. 2013a; Zhu et al. 2011). The 200–160 Ma and 100–80 Ma magmatic flare-ups occurred in the southern Lhasa subterrane (Ji et al. 2009; Ma et al. 2013a; Wen et al. 2008), whereas the 120–105 Ma magmatic flare-up mainly took place in the central and northern Lhasa subterrane (Zhu et al. 2011). The temporal and spatial distribution of the Gangdese arc magmatism is likely related to the variations of subduction angle of the Neo-Tethyan oceanic slab (Kapp et al. 2005; Ma et al. 2013b).

The Lilong lower crustal section of the Gangdese arc is exposed in the southeastern Lhasa terrane (Fig. 1A). The Lilong crustal section is structurally truncated by the Dongjiu–Miling shear zone (Geng et al. 2006; Xu et al. 2012), which juxtaposes the Gangdese lower arc crust in the hanging wall over the Himalayan sequences in its footwall (Fig. 1B). The scattered metamorphic ophiolite fragments along this shear zone were suggested to be the eastward continuation of the Yarlung-Tsangpo Suture (Geng et al. 2006). The northward indentation of the Indian plate caused rapid exhumation of the Gangdese deep crust along the Dongjiu–Miling sinistral strike-slip shear

zone during the Miocene (Xu et al. 2012; Zeitler et al. 2014). Pressure and temperature estimates reveal that the exposed Lilong section represent a tilted crustal section of the Gangdese arc that is tilted to the southwest with the paleodepths decreasing from northeast to southwest (Zhang et al. 2014, 2020) (Fig. 1B). The eastern Gangdese arc is composed of the Nyingchi Complex, the Kanniang Complex, the Lilong Complex and Wolong batholith from northeast to southwest along with late Cenozoic gabbro and granite intrusions (Fig. 1B). The Nyingchi Complex consists of garnet-bearing ortho-/paragneiss, migmatite, amphibolite, schist, quartzite, and marble. The detrital zircon geochronological studies revealed that the metasedimentary rocks in the Nyingchi Complex have various protolith ages ranging from Neoproterozoic to Early Cenozoic (Dong et al. 2010a; Guo et al. 2011, 2012, 2017; Zhang et al. 2008). The protoliths of the orthogneiss in the Nyingchi Complex include Paleoproterozoic, Cambrian, Jurassic, Cretaceous and Early Paleocene granitoids (Guo et al. 2011, 2012; Lin et al. 2013; Zhang et al. 2013). The Nyingchi Complex underwent Cenozoic (~55–25 Ma) granulite- or amphibolite-facies metamorphism (Guo et al. 2012, 2019; Zhang et al. 2020). The Kanniang Complex is dominated by garnet gabbros, constituting the deepest exposed Gangdese arc crust (Guo et al. 2013; Zhang et al. 2014). The garnet gabbros have protolith ages of 93–86 Ma and metamorphic ages of 85–68 Ma (Guo et al. 2013; Zhang et al. 2014). The pressure and temperature of peak metamorphism are 9–13 kbar and 830–900 °C (Zhang et al. 2010c, 2014), respectively. The garnet gabbros have typical arc geochemical signatures and are characterized by low initial  $^{87}\text{Sr}/^{86}\text{Sr}$  ratios of 0.70433–0.70456, positive  $\epsilon_{\text{Nd}}$  of +2.7 to +4.6, and zircon  $\epsilon_{\text{Hf}}$  of +10 to +16 (Guo et al. 2013; Zhang et al. 2014).

The Lilong Complex and Wolong granitoids are the main focus of this paper. The Lilong Complex consists of arc-related ultramafic to intermediate intrusions. Previous studies revealed that the Lilong Complex formed at 95–86 Ma, and is composed of hornblende, norite, gabbro, diorite, granodiorite, and tonalite (Ma et al. 2013a, 2013b; Zhang et al. 2010b). The intermediate rocks in the Lilong Complex have high Mg# [molar Mg/(Mg + Fe) × 100] and high Sr/Y ratio, leading to the interpretation that the mafic-intermediate rocks are the products of partial



melting of the Neo-Tethyan oceanic slab (Ma et al. 2013b; Zhang et al. 2010b). The hornblendites in the Lilong Complex have similar Sr–Nd isotopic composition to those of the mafic-intermediate rocks and were considered as the complementary cumulates fractionated from a common parental magma with the mafic-intermediate rocks (Ma et al. 2013a). The high temperature recorded in the mafic-intermediate rocks led Zhang et al. (2010b) to conclude that the Lilong Complex was metamorphosed during a high temperature event related to ridge subduction, and Ma et al. (2013a) to conclude that the Lilong Complex was related to the rollback of oceanic slab. The Wolong batholith is dominantly composed of Late Cretaceous (74–84 Ma) **granodiorite and granite**, and **is intruded by** a small Eocene (35–38 Ma) granite **pluton in the east** (Fig. 1B) (Guan et al. 2012; Ji et al. 2014; Wen et al. 2008). In this study, the Wolong **granitoids refer** to the late Cretaceous **granodiorite and granite** in the Wolong batholith. The Wolong **granitoids have** low Mg#, high Sr/Y and La/Yb ratios, and **are hypothesized to be** the product of partial melting of **the thickened Gangdese arc lower crust** (Tang et al. 2019; Wen et al. 2008).

## Field relationships and petrography

### Field relationships

Field observations revealed that the Lilong Complex is dominantly composed of mafic-intermediate rocks with three small (**200–2000 m wide**) **ultramafic bodies** (Fig. 1B). The ultramafic sequence is composed of pyroxene hornblende peridotite, hornblende pyroxenite, hornblendite, and plagioclase hornblendite. Approximately 85% of the ultramafic sequence is hornblendite with decimeter- to **meter-thick** hornblende pyroxenite and plagioclase hornblendite layers (Figs. 2A and 2B). **Fresh** pyroxene hornblende peridotite samples were collected from the waste rocks that were extracted from a ~700 m long horizontal tunnel (**inaccessible**) **within the hornblendite**. The hornblende pyroxenite occurs as **30–200 cm thick** layers in the center part of the ultramafic sequence (Fig. 2A).

The transition between the hornblende pyroxenite and hornblendite is generally gradational with increasing modal amounts of amphibole and decreasing amounts of pyroxene, and these rocks in the transition zone can be classified as pyroxene hornblendite. The transition zone is 1–3 m wide. The hornblendite is characterized by its near monomineralic composition and homogeneous texture. Towards the western margin of the ultramafic rocks, irregular plagioclase hornblendite layers occur within the hornblendites. The contact between the hornblendite and plagioclase hornblendite is gradational with modal plagioclase increasing (Fig. 2B). Amphibole megacrysts (up to 5 cm) were observed within the transition from hornblendite to plagioclase hornblendite.

The mafic-intermediate sequence is composed of hornblende gabbro, hornblende gabbro, quartz diorite, and tonalite from east to west (upward in the crustal section) (Fig. 1B). The hornblende gabbro is generally homogeneous and locally exhibits a few centimeters thick magmatic layering defined by the alternation of plagioclase-poor and plagioclase-rich bands (Fig. 2C). The hornblende gabbro grades westward into hornblende gabbro. The hornblende gabbro is foliated and contains irregular hornblendite enclaves (Fig. 2D). The foliation of the hornblende gabbro is defined by elongate clusters of pyroxene and amphibole within a plagioclase matrix. The contact relationship between the hornblende gabbro and quartz diorite was not directly observed due to lack of outcrops. The quartz diorite is homogeneous and locally contains few enclaves of hornblendite and gabbro. The quartz diorite grades westward into the tonalite, through increasing quartz mode and decreasing amounts of mafic minerals.

The contacts between the hornblendite and the hornblende gabbro are sharp intrusive contacts (Fig. 2E). The hornblendites at the contact zone are medium-grained and grade into coarse-grained hornblendites away from the contact zone. Few 10–30 cm wide veins of fine-grained hornblendite crosscut the hornblende gabbro. These phenomena reveal that the ultramafic rocks intruded into the mafic-intermediate rocks of the Lilong Complex rather than being cumulates from the same parent magma as previously hypothesized (Ma et al. 2013a). Therefore,

we distinguish between the mafic-intermediate sequence and the ultramafic sequence in the Lilong Complex.

The Wolong **granitoids** are located at the west of the Lilong Complex (Fig. 1B). The contact relationship between the Wolong **granitoids** and the tonalite from the Lilong Complex was not directly observed due to lack of outcrops. The Wolong **granitoids** mainly consists of **granodiorite and granite**. The **granitoids** are crosscut by late lamprophyre dykes. The green **magmatic epidote** is ubiquitous in the entire Wolong **batholith** (Fig. 2F).

### Petrography

The pyroxene hornblende peridotites in the ultramafic sequence have medium-grained granular texture and consist of olivine (30–79 vol %), amphibole (13–21 vol %), clinopyroxene (3–52 vol %), orthopyroxene (0–7 vol %), and magnetite (0.5–5.7 vol %). Olivine occurs as euhedral to subhedral cumulate **crystals** (Fig. 3A). **Pyroxenes** commonly **occur** as irregular distributed inter-cumulus **phases** (Fig. 3A). Amphibole occurs in two forms: large (5–10 mm) subhedral discrete grains and small (<1.5 mm) anhedral inter-cumulus grains (Fig. 3A). Both orthopyroxene and amphibole contain exsolution trails of Fe–Ti oxides (Fig. 3A). The hornblende pyroxenite is medium- to coarse-grained and is composed of clinopyroxene (35–80 vol %), orthopyroxene (3–13 vol %), amphibole (14–42 vol %), magnetite (0.5–4.7 vol %) and olivine (0–18 vol %). Clinopyroxene is subhedral and contains exsolution trails of Fe–Ti oxide (Fig. 3B). Orthopyroxene is much less abundant than clinopyroxene and occurs as irregular distributed inter-cumulus phase or rims around olivine grains. Amphibole occurs as either poikilitic grains up to 2 cm in length or as an irregular interstitial phase (Fig. 3B). The poikilitic amphibole contains abundant clinopyroxene. With increasing modal abundance of amphibole, the pyroxenite grades into pyroxene hornblendite, which in turn grades into hornblendite. **The hornblendite contains 93–99 vol% amphibole, 0–6.6 vol % clinopyroxene and 0.4–1.5 vol % magnetite**. Amphibole in the hornblendite is generally euhedral, medium to extremely coarse grained (up to 5 cm). Clinopyroxene in the hornblendite is subhedral or anhedral and occurs

as inter-granular cluster or as inclusion in the amphibole (Fig. 3C). Orthopyroxene generally occurs as small inclusion in the amphibole. The plagioclase hornblendite marks the first appearance of plagioclase within the ultramafic sequence and contains euhedral amphibole grains (66–89 vol %) and interstitial anhedral plagioclase (11–34 vol %) (Fig. 3D). Magnetite and sulfides (pyrite, chalcopyrite) occur as inclusions in the amphibole throughout the entire ultramafic sequence. These petrographic observations indicate that the crystallization sequence of ultramafic sequence is olivine → pyroxene → amphibole + Fe–Ti oxides → plagioclase.

The hornblende gabbronorites in the mafic-intermediate sequence have subhedral granular texture and consist of plagioclase (15–49 vol %), orthopyroxene (3–11 vol %), clinopyroxene (11–38 vol%), amphibole (29–38 vol %) and magnetite (1.1–4.4 vol %). Plagioclases occur as granoblastic composite grains in the form of subhedral laths. Clinopyroxene and orthopyroxene have undulated margins and are rimmed by amphibole (Fig. 3E). Amphibole in the gabbronorite occurs as rims around clinopyroxene and orthopyroxene (Fig. 3E), indicating that it crystallized late with respect to the other phases. Magnetite commonly occurs as inclusion in the amphiboles (Fig. 3E). Modal abundance of pyroxene decreases gradually from gabbronorite to hornblende gabbro, whereas the amount of amphibole increases. The hornblende gabbro is composed of clinopyroxene (5–29 vol %), plagioclase (17–28 vol%), amphibole (43–75 vol%), orthopyroxene (0–0.5 vol %), and magnetite (0.4–1.2 vol%). The hornblende gabbros display a heteradcumulate texture where poikilitic amphibole encloses plagioclase, clinopyroxene, magnetite and orthopyroxene (Fig. 3F). The quartz diorite consists of plagioclase (45–51 vol %), amphibole (13–37 vol %), quartz (5–11 vol %), biotite (4–12 vol %), K-feldspar (1–6 vol %), clinopyroxene (2–9 vol%), 0–orthopyroxene (0–2 vol%), epidote (0–3.6 vol%), and magnetite (0–2.5 vol%). The tonalite is composed of plagioclase (44–57 vol %), amphibole (8–16 vol %), K-feldspar (3–6 vol %), quartz (14–24 vol %), clinopyroxene (2–9 vol %), biotite (5–19 vol %), epidote (0–5 vol %), and orthopyroxene (0–3 vol %). The accessory minerals in the quartz diorite and tonalites include zircon, apatite, sphene, and magnetite. Amphiboles in the quartz diorite

and tonalite are generally poikilitic and enclose plagioclase, clinopyroxene, orthopyroxene, and magnetite. Plagioclase inclusions in the amphibole are euhedral indicating their early crystallization (Fig. 3G). Biotite in the tonalite occurs as euhedral laths or occasionally poikilitically enclosing euhedral epidote (Fig. 3H). Epidote in the tonalite is euhedral against the biotite, but the same crystals in contact with plagioclase and quartz show embayed contacts (Fig. 3H). The textural features of epidote are consistent with those of magmatic epidote (Schmidt and Poli 2004). Based on these observations, we infer a mineral crystallization order of pyroxene → plagioclase → amphibole + Fe-Ti oxides → biotite + epidote → K-feldspar for the mafic-intermediate sequence.

The Wolong granitoids are medium- to coarse-grained and consist of plagioclase (30–44 vol%), K-feldspar (9–30 vol%), quartz (22–33 vol%), amphibole (0–3 vol%), biotite (5–8 vol%), epidote (1–2 vol%), and minor muscovite (1–2 vol%), with accessory minerals of zircon, sphene, Fe-Ti oxides, and apatite. The plagioclase is euhedral to subhedral. The K-feldspar contains inclusions of plagioclase and biotite. The magmatic epidote occurs as euhedral or subhedral grains partially enclosed by biotite.

### Analytical methods

A total 80 whole-rock major and trace element compositions, 16 whole-rock Sr-Nd and 6 zircon Hf isotopic compositions, and 8 zircon U-Pb ages for the Lilong Complex from the Gangdese arc lower crustal section are included in the presented dataset. Whole-rock samples were crushed in an alumina jaw crusher, and then powdered in an agate mill. The powders were dried overnight at 105 °C. Loss on ignition (LOI) was determined by heating the samples to 1000 °C for 2 hours. 0.6 g of dried powder was then mixed with 6 g of lithium tetraborate and fused at 1050 °C for 10 min in platinum crucibles prior to being quenched to form homogenous glass beads. Major elements were measured by Shimadzu Sequential X-ray fluorescence (XRF-1800) at the State Key Laboratory of Geological Processes and Mineral Resources (SKLGPMR), CUG, Wuhan. Precision is better than 4% and

accuracy is better than 3% for the major elements.

Whole-rock trace elements were measured by inductively coupled plasma mass spectrometry (Agilent 7500a ICP-MS) after acid digestion of the powder samples in Teflon bombs at the SKLGPMR, CUG, Wuhan. About 50 mg dried powder was weighed into a Teflon bomb. Then, HNO<sub>3</sub> (1.5 ml) and HF (1.5 ml) were added to the Teflon bomb, which was sealed in a steel jacket and heated in an oven at 190 °C for 48 hours to completely dissolve the sample. After opening the bomb and evaporating the solution to dryness on a hotplate at ~115 °C, 1 ml of HNO<sub>3</sub> was added to the Teflon bomb and evaporated to dryness again. The resultant salt was redissolved by adding ~3 ml of 30% HNO<sub>3</sub>, resealed in a steel jacket and heated in an oven at 190 °C for 12 hours. The final solution was diluted to ~100 g with a mixture of 2% HNO<sub>3</sub> for ICP-MS analysis. Standards AGV-2, BHVO-2, RGM-2, and BCR-2 were used to monitor accuracy and precision. Accuracy was typically within ±5% of the reference value precision < 3% 2sd.

Whole-rock Sr and Nd isotopic ratios were measured by a Finnigan Triton thermal ionization mass spectrometer (TIMS) at the SKLGPMR, CUG, Wuhan. <sup>87</sup>Rb/<sup>86</sup>Sr and <sup>147</sup>Sm/<sup>144</sup>Nd ratios were calculated from measured Rb, Sr, Sm and Nd concentrations by ICP-MS. The measured <sup>143</sup>Nd/<sup>144</sup>Nd and <sup>87</sup>Sr/<sup>86</sup>Sr ratios were normalized to <sup>146</sup>Nd/<sup>144</sup>Nd = 0.721900 and <sup>88</sup>Sr/<sup>86</sup>Sr = 8.375209, respectively. During the period of analysis, standard NBS987 yielded an average <sup>87</sup>Sr/<sup>86</sup>Sr ratio of 0.710239 ± 10 (2σ), and standard BCR-2 gave an average <sup>143</sup>Nd/<sup>144</sup>Nd ratio of 0.512620 ± 2 (2σ). For details of the Sr and Nd isotopic analytical procedures see (Gao et al. 2004).

Three to five kilograms mafic-intermediate rock samples and 10–20 kilograms ultramafic rock samples were crushed, and zircons were extracted using density and magnetic techniques. Zircons were handpicked and mounted in epoxy resin, polished to expose their interiors. Cathodoluminescence (CL) images were taken on a FEI Quanta 450 FEG scanning electron microscope. U–Pb ages and trace elements of zircon were measured synchronously by

laser-ablation inductively coupled plasma mass spectrometer (LA-ICP-MS) at the SKLGPMR, CUG, Wuhan. Laser sampling was performed using a GeoLas 2005 excimer ArF laser ablation system. An Agilent 7700 ICP-MS instrument was used to acquire ion-signal intensities. All analyses were conducted using a laser beam diameter of 32  $\mu\text{m}$ . Zircon 91500 was used as external standard for correcting mass discrimination and isotope fractionation. NIST610 glass was analyzed as external standards for trace-element concentration calibration. Zircon standard GJ-1 was analyzed as unknown. In the three sessions, GJ-1 gave weighted mean  $^{206}\text{Pb}/^{208}\text{U}$  ages that are statistically indistinguishable from its nominal value (Table S2). Off-line selection and integration of background and analyte signals, and time-drift correction and quantitative calibration for trace elements and U-Pb ages were performed by *ICPMSDataCal* (Liu et al. 2010). IsoPlot Ex 3.4 (Ludwig 2003) was used to plot data on U-Pb concordia diagrams and to calculate weighted mean ages.

Zircon Lu-Hf isotope analyses were measured using a Neptune Plus MC-ICP-MS coupled with a Geolas 2005 excimer ArF laser ablation system at the SKLGPMR, CUG, Wuhan. All analyses were undertaken using a laser beam diameter of 44  $\mu\text{m}$ . Detailed operating conditions for the laser ablation system and the MC-ICP-MS instrument and analytical method are the same as description by Hu et al. (2012). Off-line selection and integration of analyte signals, and mass bias calibrations were performed using *ICPMSDataCal* (Liu et al. 2010).

Amphibole compositions were measured on carbon-coated polished sections by wavelength dispersive electron microprobe (EMP) using a JEOL JXA-8230 at the Center for Global Tectonics, School of Earth Sciences, CUG, Wuhan. The EMP was operated at an acceleration voltage of 15 kV and a beam intensity of 20 nA. The amphibole was analyzed with a spot size of 2  $\mu\text{m}$ . All analyses were matrix-corrected using the ZAF (atomic number, absorption, fluorescence) correction procedure and calibrated against natural and synthetic mineral standards. The operating conditions were described in detail in Wang et al. (2019).

## Results

### Whole-rock geochemistry

#### Ultramafic sequence in the Lilong Complex

The major and trace element chemistry of the ultramafic sequence in the Lilong Complex (Fig. 4) is controlled by the mode of olivine, pyroxene, amphibole and plagioclase. The pyroxene hornblende peridotites have high Mg#, low Al<sub>2</sub>O<sub>3</sub>, Na<sub>2</sub>O and TiO<sub>2</sub>, and various SiO<sub>2</sub> and CaO (Fig. 4). As the mode of pyroxene and amphibole increase, CaO, Al<sub>2</sub>O<sub>3</sub>, TiO<sub>2</sub> and Na<sub>2</sub>O increase with the increasing SiO<sub>2</sub>, whereas the Mg# remains nearly unchanged in the hornblende pyroxenites (Fig. 4). As the mode of amphibole drastically increases, the Mg# and CaO decrease, whereas Al<sub>2</sub>O<sub>3</sub>, TiO<sub>2</sub>, and Na<sub>2</sub>O increase with decreasing SiO<sub>2</sub> in the hornblendites (Fig. 4). With the onset of plagioclase crystallization in the plagioclase hornblendite, Al<sub>2</sub>O<sub>3</sub> reaches a maximum content (Fig. 4C) with slightly decreasing Mg# (Figs. 4A). K<sub>2</sub>O content in the ultramafic sequence is very low and slightly increases with the increase in amphibole mode (Fig. 4F).

The pyroxene hornblende peridotites and hornblende pyroxenite have high Ni and Cr contents, which decrease with the decreasing olivine and clinopyroxene mode from pyroxene hornblende peridotite to hornblendites (Table S1). The ultramafic rocks display convex upward primitive mantle-normalized (McDonough and Sun 1995) rare earth element (REE) patterns (Fig. 5A) with a depletion of light REE (LREE) with respect to middle REE (MREE; (La/Sm)<sub>N</sub> = 0.3–1.0), weakly fractionated middle to heavy REE (HREE; (Gd/Yb)<sub>N</sub> = 1.2–2.6) and Eu anomalies ranging from 0.8–1.2 [Eu/Eu\* = Eu<sub>N</sub>/(0.5\*(Sm<sub>N</sub>+Gd<sub>N</sub>))]. All ultramafic rocks are enriched in incompatible trace elements with respect to primitive mantle (McDonough and Sun 1995), exhibiting positive anomalies for Ba, K, Pb and Sr, but negative anomalies for Nb, Ta, Zr, and Hf with respect to their neighboring elements (Fig. 5B). This is consistent with arc-related signature. The positive and negative Ti anomalies (Fig. 5B) are related to the different modal abundance of Fe–Ti oxides in the ultramafic rocks.



### Mafic-intermediate sequence in the Lilong Complex

For the mafic-intermediate sequence, Mg#, Al<sub>2</sub>O<sub>3</sub>, and CaO decrease with increasing SiO<sub>2</sub>, whereas K<sub>2</sub>O increase with SiO<sub>2</sub> (Fig. 4). Na<sub>2</sub>O, TiO<sub>2</sub> and P<sub>2</sub>O<sub>5</sub> originally increase until ~50 wt % SiO<sub>2</sub> and then broadly decrease with increasing SiO<sub>2</sub> (Fig. 4). CaO continuously decreases with increasing SiO<sub>2</sub> (Fig. 4C), due to the decrease in modal abundance of clinopyroxene and the decrease in anorthite content in plagioclase with progressive fractionation. TiO<sub>2</sub> increases to the highest in the hornblende gabbros and generally decreases with increasing SiO<sub>2</sub> (Fig. 4D), reflecting that TiO<sub>2</sub> is mainly controlled by amphibole and Fe–Ti oxides. Na<sub>2</sub>O rapidly increases to 4.57 wt % in the hornblende gabbros due to the increase in modal abundance of amphibole and anorthite-poor plagioclase, and then slightly decrease with decreasing in modal abundance of amphibole (Fig. 4E). K<sub>2</sub>O is strongly controlled by the biotite mode in the mafic-intermediate rocks, increasing from the biotite-poor gabbroic rocks to biotite-bearing quartz diorite and reaching maximum content in the biotite-rich tonalite (Fig. 4F).

The trace element concentrations roughly increase from hornblende gabbro, through hornblende gabbro and quartz diorite, to tonalite (Figs. 5C and 5D). The primitive mantle-normalized REE patterns (Fig. 5C) show that all mafic-intermediate rocks have modest depletion in HREE relative to MREE, but distinct enrichment in LREE relative to MREE and HREE. The hornblende gabbros have distinct positive Eu anomalies (Eu/Eu\* = 1.2–1.8; Fig. 5C), whereas the hornblende gabbros, quartz diorites and tonalites have weakly positive to negative Eu anomalies (Eu/Eu\* = 0.8–1.2). In the primitive mantle-normalized trace element diagram (Fig. 5D), the mafic-intermediate rocks exhibit enrichment in Rb, Ba, U, K and Pb, and depletion in Nb, Ta, Zr and Hf except for the tonalites which show variably enriched or depleted Zr and Hf with respect to other incompatible elements. The hornblende gabbros have pronounced positive Ti anomalies (Fig. 5D), which is consistent with the high modal abundance of Fe–Ti oxides in the hornblende gabbros. All the mafic-intermediate rocks have high Sr

(354–911 ppm), low Y (3.83–23.2 ppm), and thus high Sr/Y ratios (19–189).

### Wolong **granitoids**

The Wolong **granitoids** have high SiO<sub>2</sub> (66.0–70.2 wt %), Al<sub>2</sub>O<sub>3</sub> (16.4–18.1 wt %), Na<sub>2</sub>O (4.25–5.40 wt %) and K<sub>2</sub>O (1.64–3.35 wt %) contents and low Mg# (30–41) (Fig. 4). They are **slightly** per-aluminous with A/CNK (molar Al<sub>2</sub>O<sub>3</sub>/(CaO + Na<sub>2</sub>O + K<sub>2</sub>O)) values of 1.01–1.37. The Wolong granites display variably fractionated HREE patterns ((Dy/Yb)<sub>N</sub> = 1.1–2.0), strongly enrichment in LREE relative to HREE ((La/Yb)<sub>N</sub> = **11–53**), and weakly negative to positive Eu anomalies (Eu/Eu\* = **0.9–1.6**) in the **primitive mantle**-normalized REE diagram (Fig. 5E). Combined with published data, the Wolong granites can be divided into the high and low (Dy/Yb)<sub>N</sub> groups (Fig. 5E). Primitive mantle-normalized trace element patterns are characterized by enrichment in Rb, Ba, U, K, Pb and Sr, and depletion in Nb, Ta, and Ti with respect to adjacent elements (Fig. 5F).

### Zircon U-Pb geochronology

**Five samples** from mafic-intermediate sequence, two hornblendite **samples** from the ultramafic sequence and one Wolong **granitoid sample** were selected for LA-ICP-MS zircon U-Pb dating. The representative zircon CL images are shown in Fig. 6. Zircon dating results are presented as concordia diagrams in Fig. 7 with the detailed data set being listed in supplementary Table S2.

### **Mafic-intermediate sequence**

Zircons from the gabbro-norite (14GT035) **are euhedral and are 50–150 μm long. They display sector or broad zoning in the CL images (Fig. 6A). They have Th of 55.2–209 ppm and U of 71.9–290 ppm with Th/U ratios of 0.6–1.2 (Table S2), indicating a magmatic origin. Twenty analyses of zircon from sample 14GT035 yield a**

weighted mean  $^{206}\text{Pb}/^{238}\text{U}$  age of  $92.1 \pm 0.6$  Ma (MSWD = 1.04; Fig. 7A). Zircons in the quartz diorite sample 18GT304 are euhedral or subhedral with crystal length of 100–250  $\mu\text{m}$ . They show banded zoning in the CL images (Fig. 6B) and have variable Th (56.1–280 ppm) and U (54.9–320 ppm) contents, with Th/U ratios of 0.4–1.0. Twenty analyses yield a weighted mean  $^{206}\text{Pb}/^{238}\text{U}$  age of  $90.4 \pm 0.5$  Ma (MSWD = 0.76; Fig. 7B). Zircons from three tonalite samples (T1372, 16GT059 and 16GT063) are euhedral in shape and 80–250  $\mu\text{m}$  in length. Most zircons display sector zoning, banded zoning or oscillatory zoning in the CL images (Figs. 6 C–E). All analyses of zircons from the tonalite samples have Th of 58.6–761 ppm and U of 90.7–1051 ppm with high Th/U ratios of 0.3–1.2. Of twenty zircons from sample T1372, nineteen analyses are concordant and yield a weighted  $^{206}\text{Pb}/^{238}\text{U}$  mean ages of  $91.4 \pm 0.7$  Ma (MSWD = 1.3; Fig. 7C). Of twenty analyses of zircons from sample 16GT059, nineteen analyses are concordant and gave a weighted mean  $^{206}\text{Pb}/^{238}\text{U}$  age of  $90.5 \pm 0.8$  (MSWD = 2.8; Fig. 7D). Of twenty zircons from sample 16GT063, nineteen concordant analyses gave a weighted mean  $^{206}\text{Pb}/^{238}\text{U}$  age of  $88.6 \pm 0.7$  Ma (MSWD = 1.3; Fig. 7E).

### Ultramafic sequence

Seven and seventeen zircons were separated from the hornblende sample T1365 and 14GT033, respectively. Zircons in the hornblendites are euhedral and small with crystal length of 30–80  $\mu\text{m}$ . They display sector zoning of igneous zircon in the CL images (Figs. 6F and 6G). Only three zircons from sample T1365 and seven zircons from sample 14GT033 are large enough for LA-ICP-MS analysis after polish. Three analyses of zircons from sample T1365 have Th of 59.0–162 ppm and U of 89.1–254 ppm with Th/U ratios of 0.6–1.0 and gave a weighted mean  $^{206}\text{Pb}/^{238}\text{U}$  age of  $85.9 \pm 2.3$  Ma (MSWD = 0.01) (Fig. 7F). Zircons from sample 14GT033 have Th of 68.7–258 ppm and U of 131–254 ppm with Th/U ratios of 0.5–1.0. Of seven analyses from sample 14GT033, five analyses are concordant and gave a weighted mean  $^{206}\text{Pb}/^{238}\text{U}$  age of  $85.4 \pm 1.4$  Ma (MSWD = 0.31) (Fig. 7G).

### Wolong granitoids

Zircons from the Wolong granitoid sample T914 are euhedral and have length of 150–300  $\mu\text{m}$ . In the CL images (Fig. 6H), most zircons show oscillatory zoning. Zircons from sample T914 have Th of 88.0–752 ppm and U of 206–1274 ppm with Th/U ratios of 0.4–0.8. Seventeen analyses of zircons yield a weighted mean  $^{206}\text{Pb}/^{238}\text{U}$  age of  $79.9 \pm 0.6$  Ma (MSWD = 1.05) (Fig. 7H).

### Sr-Nd-Hf isotopic compositions

Whole-rock Sr–Nd and zircon Hf isotopic data are provided in supplementary Tables S3 and S4, respectively. Whole-rock initial Sr–Nd isotopic ratios for all lithological sequences from the Lilong Complex and the Wolong granite are calculated using an age of 90 Ma. Zircon  $\epsilon_{\text{Hf}}(t)$  value is calculated using the weighted mean age of individual sample. The mafic-intermediate and ultramafic sequences display similar whole-rock Sr–Nd and zircon Hf isotopic compositions. The ultramafic rocks have  $\epsilon_{\text{Nd}}(t)$  values of +2.8 to +4.0 and initial  $(^{87}\text{Sr}/^{86}\text{Sr})_i$  of 0.704267–0.704572, which overlap with that of the mafic-intermediate rocks having  $\epsilon_{\text{Nd}}(t)$  values of +3.2 to +4.3, and initial  $(^{87}\text{Sr}/^{86}\text{Sr})_i$  of 0.704198–0.704557 (Figs. 8A). The zircon  $\epsilon_{\text{Hf}}(t)$  values are +12.2 to +14.0 for ultramafic rocks and +11.3 to +14.3 for mafic-intermediate rocks (Fig. 8B). The Wolong granitoids have slightly lower zircon  $\epsilon_{\text{Hf}}(t)$  values of +8.4 to +10.3 than those of the Lilong Complex (Fig. 8B).

### Amphibole barometry

The mineral compositions of amphibole are given in Table S5. Amphiboles from the ultramafic and mafic-intermediate sequences in the Lilong Complex are pargasite or Mg-hornblende according to the nomenclature of

(Hawthorne et al. 2012). The tonalite and quartz diorite from the mafic-intermediate sequence of Lilong Complex contain the mineral assemblage of plagioclase, K-feldspar, amphibole, biotite, epidote, magnetite, sphene, and quartz, which allow us to use Al-in-hornblende geobarometer (Schmidt 1992) to determine their intrusion pressures. Pressure were calculated from hornblende rim compositions. Samples T744 and T1372 from Lilong village (Fig. 1B) yield pressures of  $6.3 \pm 0.2$  kbar and  $6.1 \pm 0.3$  kbar, respectively, consistent with the presence of magmatic epidote (Schmidt and Poli 2004). About 7 km to the northeast (Fig. 1B), sample 16GT059 collected near the bottom of the tonalite pluton yield pressure of  $7.4 \pm 0.2$  kbar. Pressure calculated on quartz diorite sample 14GT042 collected about 2 km to the east of sample 16GT059 yields pressure of  $7.3 \pm 0.4$  kbar. Calculated pressure increases to  $8.2 \pm 0.4$  kbar for sample 16GT053 collected near the bottom of quartz diorite pluton (Fig. 1B). The pressure estimates for different samples have small errors (0.2–0.4 kbar), which resulted from the homogeneity of amphibole rim compositions. Pressure estimates for the gabbroic rocks in the mafic-intermediate sequence are not straightforward. The garnet gabbros from the Kanniang Complex underlying the Lilong Complex formed at pressures of ~9–13 kbar (Zhang et al. 2010, 2014), which provides the maximum intrusion pressure for the gabbroic rocks. The overlying quartz diorite provides the minimum intrusion pressure of ~8.2 kbar for the gabbroic rocks. Accordingly, the intrusion pressures of the gabbroic rocks were 8.2–9.0 kbar.

The intrusion pressure of the ultramafic sequence is rather difficult to constrain due to the lack of appropriate mineral assemblages for barometry. Amphiboles in the pyroxene hornblende peridotite coexist with olivine, orthopyroxene, and clinopyroxene, and have high Mg# of 80–84 (Table S5). Our petrographic observations show that the amphibole preceded the plagioclase appearance in the ultramafic sequence. This allows us to use the amphibole Mg# and Al<sup>VI</sup> geobarometers of Krawczynski et al. (2012) to estimate the pressure of the pyroxene hornblende peridotite. We need to estimate the oxygen fugacity ( $fO_2$ ) of the magma before using the Mg# amphibole barometer. The  $fO_2$  evolution modeling of closed-system equilibrium crystallization experiment has

shown that the  $fO_2$  of the primary high-Mg basalt increase from NNO-0.31 to NNO+1.45 before amphibole saturation (Ulmer et al. 2018). The abundant crystallization of magnetite and amphibole in the pyroxene hornblende peridotite indicates high  $fO_2$  (Carmichael 1991; Ulmer et al. 2018). Thus, a  $fO_2$  of NNO+1.5 is used to calculate the pressure. The most Mg-rich amphiboles (Mg# = 82.7–84.4) in the pyroxene hornblende peridotite sample 15GT033 yield pressures of  $8.4 \pm 1.2$  kbar and  $9.0 \pm 0.6$  kbar by using the Mg# and  $Al^{VI}$  geobarometers (Krawczynski et al. 2012), respectively. The average pressure of the Mg# barometer and the  $Al^{VI}$  barometers is ~8.7 kbar (Table S5) which is considered as the best intrusion pressure estimate of the ultramafic sequence.

## Discussion

### Wet and damp fractionation sequences in the Lilong Complex

Our field and petrographic observations reveal that the mafic-intermediate and ultramafic sequences in the Lilong Complex represent two different igneous crystallization sequences. First, the cross-cutting intrusive contact (Fig. 2A) indicates that the mafic-intermediate sequence was emplaced before the ultramafic sequence. This is corroborated by younger zircon U-Pb ages from the ultramafic sequence (85–86 Ma) compared with the mafic-intermediate sequence (89–92 Ma) (Fig. 7). Furthermore, petrographic observations indicate that the mafic-intermediate and the ultramafic sequences have different mineral crystallization sequences. Amphibole precedes plagioclase in the ultramafic sequence, whereas plagioclase precedes amphibole in the mafic-intermediate sequence. The variations in  $H_2O$  content of primitive arc magma have large effects on the crystallization sequence. High  $H_2O$  content in the melt suppresses plagioclase crystallization and promotes early amphibole crystallization at lower crust pressures (Krawczynski et al. 2012; Müntener et al. 2001; Sisson and Grove 1993). The early crystallization of plagioclase in respect to amphibole in the mafic-intermediate sequence indicates that their

parental magma had lower H<sub>2</sub>O content compared to the magma parental to the ultramafic sequence. By contrast, the co-precipitation of amphibole with olivine and pyroxene in the peridotite and abundant amphibole-rich cumulates before the appearance of plagioclase in the ultramafic sequence are consistent with the crystallization sequence of H<sub>2</sub>O-saturated crystallization experiments (Krawczynski et al. 2012; Ulmer et al. 2018). Despite similar Sr–Nd–Hf isotopic compositions (Fig. 8), the mafic-intermediate and the ultramafic sequences formed from distinct parental melts that have different initial water content. We consider the mafic-intermediate and ultramafic sequences to represent damp (low H<sub>2</sub>O) and wet (H<sub>2</sub>O saturated) fractionation sequences of arc magmas, respectively.

#### Wet fractionation of the ultramafic sequence

Field and petrographic observations reveal that the ultramafic sequence can be ascribed to a fractionation sequence defined by olivine → pyroxene → amphibole + Fe–Ti oxides → plagioclase. This crystallization sequence is in line with the fractional crystallization experiments on H<sub>2</sub>O-saturated primary arc magmas at lower crustal conditions (Krawczynski et al. 2012; Ulmer et al. 2018). The high Mg# (80–84) amphibole coexisting with olivine is a strong evidence for H<sub>2</sub>O-saturated condition (Krawczynski et al. 2012). We note that the presence of mineral assemblage consistent with water saturated magma at the pressure of ~8–10 kbar implies water concentration of ~15–20 wt% in the melt (Mitchell et al. 2017).

The pyroxene hornblende peridotite and hornblende pyroxenite are characterized by a substantial increase in SiO<sub>2</sub> at relatively constant Mg# (Fig. 4A). The hornblendites display a decrease in SiO<sub>2</sub> accompanied by a strong decrease in Mg# and strong increase in Al<sub>2</sub>O<sub>3</sub>, TiO<sub>2</sub>, and Na<sub>2</sub>O (Fig. 4). The CaO drastically increases with increasing SiO<sub>2</sub> from the hornblende pyroxene peridotite to hornblende pyroxenite, and then decreases with decreasing SiO<sub>2</sub> for the hornblendites, forming an anticlockwise evolution track (Fig. 4B). The major element

signature of the ultramafic sequence matches the cumulate lines of descent of medium- to high-pressure hydrous fractional experiments (Müntener and Ulmer 2018).

#### Damp fractionation of the mafic-intermediate sequence

Petrographic observations indicate that the mafic-intermediate sequence can be ascribed to a fractionation sequence defined by pyroxene → plagioclase → amphibole + Fe-Ti oxides → biotite + epidote → K-feldspar → quartz. The hornblende gabbro has high Mg#, high CaO (Figs. 4A and 4B) and Sr contents, and positive Eu anomalies (Fig. 5C), implying that pyroxenes and plagioclases fractionation played an important role in the early magma evolution. The low (Gd/Yb)<sub>N</sub> ratios (Fig. 9A) of the hornblende gabbros indicate that the amphibole is not an early cumulate phase, which is consistent with that the amphibole formed through reactions between cumulus pyroxenes and **hydrous** evolved melts **and/or** aqueous fluid (Fig. 3E). The hornblende gabbros display significant decrease in Mg# and CaO, and substantial increase in TiO<sub>2</sub> and Na<sub>2</sub>O contents (Fig. 4) and (Gd/Yb)<sub>N</sub> ratios (Fig. 9A) at relatively constant SiO<sub>2</sub>, reflecting that the **accumulation** of amphibole and Fe-Ti oxides. The quartz diorite and tonalite show decrease in Mg#, Al<sub>2</sub>O<sub>3</sub>, CaO, TiO<sub>2</sub>, and Na<sub>2</sub>O with increasing SiO<sub>2</sub> (Fig. 4), and display negative correlations of (Gd/Yb)<sub>N</sub> vs SiO<sub>2</sub> (Figs. 9A) and Sr/Y vs SiO<sub>2</sub> (Figs. 9B), indicating the fractionation of plagioclase and amphibole. Amphibole became the dominant crystallization phase in the hornblende gabbro, quartz diorite and tonalite, **indicating that the melts parental to these rocks reached at 4 wt% water (Alonso-Perez et al. 2009)**. This is consistent with the generally incompatible behavior of H<sub>2</sub>O in magmas which results in an increase in H<sub>2</sub>O content with differentiation. K<sub>2</sub>O contents increase with increasing SiO<sub>2</sub>, consistent with the crystallization of biotite and K-feldspar. The fractionation trend of K<sub>2</sub>O vs SiO<sub>2</sub> (Fig. 4F) is similar to the trend observed in liquid compositions of low H<sub>2</sub>O fractionation sequence (the Chilas Complex) in the Kohistan arc (Jagoutz et al. 2011). The whole rock geochemistry of the mafic-intermediate sequence can be



interpreted in terms of cumulate and melt compositions belonging to a single liquid line of descent. Although the ultramafic cumulates are absent in the mafic-intermediate sequence, the geochemical signatures of the mafic-intermediate sequence are consistent with the lines of descent of medium- to high-pressure low-H<sub>2</sub>O fractional experiments (Müntener and Ulmer 2018).

### Origin of the Wolong granitoids

Partial melting of amphibolite in the lower crust (e.g., Clemens and Vielzeuf 1987; Rapp and Watson 1995) or hydrous medium- to high-pressure magma fractional crystallization (e.g., Jagoutz 2010; Jagoutz and Klein 2018; Nandedkar et al. 2014) have been proposed as the main processes responsible for the formation of granitoids. The Wolong granitoids have high SiO<sub>2</sub>, low Mg# (30–41), weakly negative to positive Eu anomalies ( $\text{Eu}/\text{Eu}^* = 0.86\text{--}1.57$ ), high Sr/Y and  $(\text{La}/\text{Yb})_N$  ratios, positive  $\epsilon_{\text{Nd}}(t)$  and  $\epsilon_{\text{Hf}}(t)$  values (Fig. 8), and low initial  $(^{87}\text{Sr}/^{86}\text{Sr})_i$  (Ji et al. 2014; Tang et al. 2019; Wen et al. 2008; this study). These geochemical features have led to the interpretation that the Wolong granitoids are the products of partial melting of the thickened juvenile lower crust (Ji et al. 2014; Tang et al. 2019; Wen et al. 2008). Zircon U-Pb geochronologic data indicate that the Wolong granitoids were formed between 74–84 Ma (Fig. 10). The absence of coeval mafic magmatism in the Gangdese arc is the main argument against arc magma generating the Wolong granitoids via fractional crystallization (Ji et al., 2014; Tang et al., 2020). However, lack of mafic magmatism is in conflict with a local external source of heat, generally assumed to be the contemporary mantle-derived magma, required to cause the lower crust to melt (Dufek and Bergantz 2005). In addition, the Wolong granitoids exhibit a significant variation in  $(\text{Dy}/\text{Yb})_N$  ratio (Fig. 9C). The low  $(\text{Dy}/\text{Yb})_N$  group from the Wolong granitoids show negative correlation between the  $(\text{La}/\text{Sm})_N$  and  $(\text{Dy}/\text{Yb})_N$  (Fig. 9C), indicating significant amphibole restite. Dehydration melting experiments show that the amount of amphibole diminishes with increasing degree of partial melting and that the amphibole is generally consumed after 6–15 vol%

melting (Beard and Lofgren 1991; Rapp et al. 1991). During lower crustal partial melting, melts became SiO<sub>2</sub>-poorer with increasing degree of partial melting (Jagoutz and Klein 2018). However, the Wolong granitoids are characterized by increasing SiO<sub>2</sub> and decreasing MgO with time (Fig. 11A and 11B) implying that these melts would have formed during cooling of the lower crust and the melts from the initial heating event are not observed. Decreasing MgO with younger age is a hallmark of basalt differentiation where melts evolved with time due to fractional crystallization.

Indeed, fractionation crystallization process is more efficient than partial melting for the formation of granitoids in subduction systems (Jagoutz and Klein 2018; Müntener and Ulmer 2018). The initial H<sub>2</sub>O contents of mantle-derived melts play an important role in producing volume of granitoids (Müntener and Ulmer 2018). For the damp magma, the early crystallization of plagioclase and pyroxene is inefficient to produce volumetrically significant SiO<sub>2</sub>-rich derivative liquids as cumulates and melts have very similar SiO<sub>2</sub> contents (Davidson et al. 2007; Jagoutz et al. 2013; Müntener and Ulmer 2018). By contrast, the cumulates in the wet fractionation system contain various proportions of SiO<sub>2</sub>-poor minerals like amphibole, garnet, high-An plagioclase, and Fe-Ti oxides, which is sufficient to push derivative liquids to high SiO<sub>2</sub> contents (Jagoutz et al. 2013; Müntener and Ulmer 2018). As stated above, both a damp and wet fractionation sequences are observed in the Lilong Complex. The Wolong granitoids cannot be directly derived from the damp fractionation sequence of the Lilong Complex because: (1) the 74-84 Ma Wolong granitoids are systematically younger than the 85-94 Ma mafic-intermediate sequence (Fig. 10); (2) the Wolong granitoids deviate from the evolution trend of the mafic-intermediate sequence (Fig. 4) and the liquid lines of damp fractional crystallization experiments (Fig. 12). However, the whole-rock composition of the Wolong granitoids match well with the liquid line of descent of the wet fractionation experiments (Fig. 12). The Wolong granitoids, for a given K<sub>2</sub>O content, have significantly higher SiO<sub>2</sub> content than those of the tonalites in the Lilong Complex (Fig. 4F), which is similar to the fractionation path of the hydrous arc magma in the Kohistan

arc (Jagoutz et al. 2011).

The high  $(\text{Dy}/\text{Yb})_N$  Wolong granitoids have a positive correlation between  $(\text{La}/\text{Sm})_N$  and  $(\text{Dy}/\text{Yb})_N$  (Fig. 9C), indicating that the formation of the high  $(\text{Dy}/\text{Yb})_N$  granitoids were controlled by garnet-dominated fractionation at high pressures. In contrast, the low  $(\text{Dy}/\text{Yb})_N$  Wolong granitoids have a negative correlation between  $(\text{La}/\text{Sm})_N$  and  $(\text{Dy}/\text{Yb})_N$  (Fig. 9C), indicating that the low  $(\text{Dy}/\text{Yb})_N$  granitoids were controlled by amphibole-dominated fractionation at medium pressures. In the Lilong crustal section, the 85–86 Ma ultramafic sequence in the Lilong Complex probably represents the cumulate of wet arc magma from which the early stage (~84 Ma) Wolong granitoids originated (Fig. 10). However, the intermediate rocks and garnet-rich cumulates related to the wet fractionation sequence were not observed in the exposed Lilong crustal section. The intermediate rocks and garnet-rich cumulates may exist but could be difficult to find due to lack of outcrops. In addition, the garnet-rich cumulates are generally denser than residual upper mantle and more likely have detached from the Gangdese arc lower crust (Jagoutz and Behn 2013). Nevertheless, more work is needed to test our speculation in the future.

From east to west, the  $\epsilon_{\text{Nd}}(t)$  values of the Wolong granitoids decrease and initial  $(^{87}\text{Sr}/^{86}\text{Sr})_i$  ratios increase (Fig. 11C and 11D). The granitoid sample isotopically most enriched is in the vicinity of the 352–355 Ma Langxian granodiorites (Ji et al. 2012; Tang et al. 2019). The spatial trends of Sr–Nd isotopic compositions suggest increasing crustal assimilation towards the west, which is confirmed by the increasing occurrence of 293–376 Ma inherited zircons (Tang et al. 2019). For simple endmember modeling (Fig. 8A), the Sr–Nd isotopic variation of the Wolong granites can be generated by mixing of most depleted melts with a small amount (<10 %) crustal assimilation. Based on these observations, we consider that the Wolong granitoids were probably derived from fractional crystallization of wet arc magma modified due to intra-crustal assimilation in the upper crust during emplacement.

### Construction of the Gangdese arc deep crust

Pressure estimates for the exposed Late Cretaceous Gangdese arc deep crustal section show that it exposes a near complete section of arc lower crust. The arc section in the Lilong area is composed of the Kanniang Complex, the Lilong Complex and the Wolong granitoids (Fig. 1B). Pressure estimates for the garnet gabbros in the Kanniang Complex are 9–13 kbar (~31–42 km) (Zhang et al. 2010c, 2014). Within the Lilong Complex, pressure decreases from ~9 kbar (~31 km depth) at the base gabbro to ~6.1 kbar (~21 km depth) at the top tonalite (Fig. 1C). The ubiquitous magmatic epidote in the Wolong granitoids (Wen et al. 2008) indicates its crystallization pressure is >5 kbar (>17 km) (Schmidt and Poli 2004). Taking the crystallization pressure of tonalite as the maximum pressure, the Wolong granitoids probably formed at 5–6 kbar (17–21 km). Thus, the Lilong Gangdese arc crustal section exposes a near complete section extending from ~42–17 km paleodepth (Fig. 1C).

As stated above, two different fractionation sequences of arc magma are observed in the Lilong Gangdese arc crustal section. The mafic-intermediate sequence in the Lilong Complex resulted from damp fractionation, whereas the ultramafic sequence in the Lilong Complex and the Wolong granitoids resulted from wet fractionation of arc magmas. The garnet gabbros in the Kanniang Complex have consistent protolith crystallization ages (Fig. 10) and similar geochemical and Sr–Nd–Hf isotopic compositions to the mafic-intermediate sequence in the Lilong Complex (Fig. 8) (Guo et al. 2013; Zhang et al. 2014), indicating that they formed under the same geodynamic setting and were derived from the same mantle source. The Kanniang Complex and mafic-intermediate sequence of the Lilong Complex constitute ~95% of the Gangdese arc lower crust, indicating that the Gangdese arc lower crust mainly derived from damp fractionation. It probably is because the liquids derived from damp melts are more viscous than those derived from hydrous melts that the liquids stagnate in the lower crust (Jagoutz et al. 2011, 2013). The Wolong granitoids derived from wet fractionation separated from their source region more easily and thus formed the Gangdese arc upper crust. This is similar to the Kohistan and Talleetna oceanic arc lower crust

(Jagoutz et al. 2011). The garnet-rich cumulates related to wet high-pressure fractionation sequence and ultramafic cumulates related to damp fractionation sequence are absent in the exposed Gangdese lower crust. **These cumulates may have been removed by the Dongjiu-Miling shear zone (Fig. 1B). More than likely, these cumulates delaminated back into the mantle** since they are generally denser than residual upper mantle (Jagoutz and Behn 2013).

Our new LA-ICP-MS zircon U-Pb ages, together with previously published LA-ICP-MS and SIMS zircon U-Pb ages for the Lilong crustal section (Guo et al. 2013; Ji et al. 2014; Ma et al. 2013a, 2013b; Tang et al. 2019; Wen et al. 2008; Zhang et al. 2020; Zhu et al. 2011), place tight temporal constraints on the incremental assemblage of the deep crust of the Gangdese arc (Fig. 10). The garnet gabbros in the Kanniang Complex mainly have protolith ages of 86–93 Ma (Fig. 10). The gabbroic rocks, quartz diorite, and tonalite from the mafic-intermediate sequence of Lilong Complex have consistent crystallization ages of 89–94 Ma, 87–95 Ma, and 85–92 Ma (Fig. 10). The ultramafic sequence in the Lilong Complex and the Wolong **granitoids have younger** crystallization ages of 85–86 Ma and **74–84 Ma** (Fig. 10), respectively. Based these observations, we consider that the Lilong Gangdese arc deep crust was built mainly through fractionation of the early (85–95 Ma) damp and late (**74–86 Ma**) wet arc magmas.

### **Seismic properties of the Gangdese deep crust**

**We calculate a seismic wave speeds profile of the Gangdese deep crust to compare the Gangdese arc to measurements of continental crust.** To calculate the equilibrium mineral assemblage, densities, and seismic velocities for each composition, we use the Gibbs free energy minimization routine *Perple\_X* (Connolly 2009). All thermodynamic modelling was performed in the 10 component NCKFMASHTO (Na<sub>2</sub>O–CaO–K<sub>2</sub>O–FeO–MgO–Al<sub>2</sub>O<sub>3</sub>–SiO<sub>2</sub>–H<sub>2</sub>O–TiO<sub>2</sub>–O<sub>2</sub>) compositional system and the following solution models: augite and

hornblende (Green et al. 2016); garnet, orthopyroxene, biotite, staurolite, cordierite, and chlorite (White et al. 2014a); olivine and epidote (Holland and Powell 2011); magnetite-spinel (White et al. 2002); ilmenite-hematite (White et al. 2000); C1 plagioclase and K-feldspar (Holland and Powell 2003); and muscovite-paragonite (White et al. 2014b). A melt solution model was excluded to increase calculation efficiency and calculate the subsolidus density and seismic velocity. Pure phases included quartz, rutile, titanite, and aqueous fluid. We assume a minimum equilibrium temperature of 500°C, a reasonable lower bound for net transfer reactions under hydrous crustal conditions (Austrheim 1998). For all Perple\_X calculations, we assume that 25 mol % of the total iron oxide is ferric (Cottrell and Kelley 2011; Kelley and Cottrell 2012); varying this value to 15 or 35 mol% changed seismic velocities by less than 1%. Seismic velocities are calculated using a compilation of mineral properties (Abers and Hacker 2016) implemented into Perple\_X with the alpha-beta quartz implementation used by Jagoutz and Behn (2013). Mineral assemblage, density, and seismic velocity are calculated using pressures derived from geothermobarometry of the observed mineral compositions and temperature calculated along steady-state 60 mW/m<sup>2</sup> geotherm. The calculated results are provided in supplementary Table S6.

The calculated seismic properties of the Gangdese arc deep crust agree with those of the averaged continental crust (Fig. 13) (Christensen and Mooney 1995). Additionally, the P-wave speeds ( $V_P$ ) of the Gangdese arc deep crust are lower than that of active oceanic arcs (Fig. 13) (Calvert 2011). The Wolong granites have constant  $V_P$  of ~6.25 km/s and density of ~2.70 kg/m<sup>3</sup> from ~17 to 21 km depth (Fig. 13). With the occurrence of tonalite, the density increases to ~2.85 kg/m<sup>3</sup> and  $V_P$  increases to 6.32 km/s at ~22 km (Fig. 13). From ~21 to 27 km depth (Fig. 13),  $V_P$  gradually increase from ~6.3 to ~6.5 km/s, and density increase from 2.75 to 2.92 kg/m<sup>3</sup>. The  $V_P$  and density rapidly increase to ~6.7 km/s and ~3.00 kg/m<sup>3</sup> at 28.5 km depth corresponding the occurrence of gabbroic rocks (Fig. 13). The fossil oceanic (Kohistan and Talleetna) and continental (Gangdese and Famatinian) arc crustal sections display a significant discontinuity in  $V_P$  between the intermediate rocks (6.0–6.5 km/s) and underlying

mafic rocks (6.7–7.1 km/s), although the depths of the discontinuities are different from one arc to another. The occurrence of the high density (3.00–3.19 kg/m<sup>3</sup>) ultramafic intrusion in the gabbroic rocks result in a spike of  $V_P$  (~6.9 km/s) at ~29 km depth (Fig. 13). The gabbros, gabbro-norites and garnet gabbros under the ultramafic intrusion have the density of 3.02–3.17 kg/m<sup>3</sup> and  $V_P$  ranging from 6.7–6.9 km/s from 31–42 km depth (Fig. 13). Compared with the Kohistan and Talkeetna arcs (Jagoutz and Behn 2013), the density-unstable ultramafic cumulates/garnet granulites are missing in the base of the Gangdese arc lower crust (Fig. 13). The density and  $V_P$  of the Gangdese arc lower crust are lower than those of the underlying mantle, indicating that the Late Cretaceous Gangdese arc lower crust underwent significant density sorting.

#### The composition of the Gangdese arc lower crust

The composition of arc lower crust depends on the definition of the lower crust because the depth and thickness of the arc lower crust vary regionally. We define the Gangdese arc lower crust as the lower half of the Late Cretaceous Gangdese arc crust. For the Lilong section, the Lilong and Kanniang Complexes make up the lower half of the Late Cretaceous Gangdese arc crust (Fig. 13). The crust-mantle boundary was not observed in the Lilong section, so it is unclear how much lower crust was removed by delamination or shearing along the Dongjiu-Miling shear zone (Fig. 1B). The crustal thickness of the Late Cretaceous Gangdese arc was ~42 km based on available pressure estimates of the garnet gabbros from the Kanniang Complex in the Lilong section (Zhang et al. 2014), indicating limited loss of the lower crust in the Lilong section due to later deformation related to India-Asian collision. We calculate the bulk Gangdese arc lower crust composition from geobarometrically derived thicknesses of the Kanniang and Lilong Complexes and compare it with composition estimates of LCC. A total of 195 samples were compiled to calculate the composition of the Gangdese arc lower crust (Table S7). The geobarometrically inferred thicknesses, the densities, and the average geochemical compositions of all units of the

Gangdese arc lower crust are given in the Table S7.

The composition of the Kanniang Complex was calculated by averaging 27 whole-rock analyses which distributed from the base to the top of the Kanniang Complex. No significant chemical stratigraphy occurs within the Kanniang Complex (Table S7). Thus, we averaged the available 27 whole-rock compositions, yielding a basaltic andesite with SiO<sub>2</sub> of ~53.0 wt% and Mg# of ~47. For the average bulk composition of the Lilong Complex, we estimate that the ultramafic sequence makes up ~10% of the Lilong Complex and the mafic-intermediate sequence the remaining ~90% based on field mapping. The relative thickness of each lithological unit from the mafic-intermediate sequence of the Lilong Complex was based on our amphibole geobarometric constraints. We calculated averages for each rock type and a weighted average for the mafic-intermediate sequence, which resulted in a bulk composition of the mafic-intermediate sequence of ~57.1 wt% SiO<sub>2</sub> and an Mg# of ~49 (Table S7). The bulk composition of the ultramafic sequence in the Lilong Complex was calculated by averaging 43 whole-rock compositions, taking into account the abundance of ~84.5% hornblende, ~4.1% peridotite, ~10.4% pyroxenite, and ~1% plagioclase hornblende based on field mapping. Our estimated bulk composition of the ultramafic sequence (Table S7) is basaltic (~47.7 wt% SiO<sub>2</sub> and Mg# of ~72) and is depleted in highly incompatible elements compared with the estimates for the mafic-intermediate sequence of the Lilong Complex and the Kanniang Complex (Fig. 14A). In the LCC-normalized diagram (Fig. 14A), the pattern of the ultramafic sequence is approximately complementary to that of the Wolong pluton, further supporting our inferences that the Wolong pluton was derived from fractional crystallization of wet arc magma. Our estimated bulk composition of the entire Lilong Complex (Table S7) is basaltic andesite (SiO<sub>2</sub> ~56.2 wt% and Mg# ~55).

Finally, the average bulk lower crust composition of the Gangdese arc was calculated from the geobarometrically derived thickness of the Lilong and Kanniang Complexes, which make up ~48 % and ~52% of the Gangdese arc lower crust, respectively. There is an uncertainty in the thickness of the Kanniang Complex as



its base was truncated by the Dongjiu-Miling shear zone (Fig. 1B). However, the Kanniang Complex displays similar chemical composition to our estimate of the Gangdese arc lower crust (Fig. 14A), indicating that the variation in thickness of the Kanniang Complex cannot significantly influence our estimate of the Gangdese lower crust. Thus, our estimate of the Gangdese arc lower crust is robust.

The average composition of the Gangdese arc lower crust is **basaltic andesite** with SiO<sub>2</sub> of ~54.6 wt % and Mg# of ~51 (Table S7). These calculated compositions are significantly more mafic than the estimate of the Gangdese lower crust by Zhang et al. (2020). The most important factor for this difference is that ~31% of the whole-rock data compiled by Zhang et al. (2020) are granitic rocks from the Cenozoic Nyingchi Complex and the Wolong **granitoids**. Unlike the calculation of Zhang et al. (2020), the Nyingchi Complex and Wolong **granitoids** are excluded in our calculation as the Nyingchi Complex mainly formed after the India-Asian collision (Guo et al. 2012; Zhang et al. 2020) and the Wolong **granitoids** represent the upper crust of the Gangdese arc. Additionally, our estimate is more robust than Zhang et al. (2020) since we weighted our average composition by the proportion of different lithology units.

The average composition of the Gangdese arc lower crust is similar to the estimates of the lower continental crust (LCC; Hacker et al. 2015; Rudnick and Gao 2014). The difference of major and trace elements is generally within 10–50 rel% between the Gangdese arc lower crust and the LCC of Rudnick and Gao (2014), and is within 10–30 rel% between the Gangdese arc lower crust and the newly estimated LCC of Hacker et al. (2015). The Gangdese arc lower crust has 35–64 % lower Nb and Ta with respect to the LCC of Rudnick and Gao (2014), which could be explained by **the absence** of within-plate mafic rocks in the **Lilong crustal section**. Compared with the LCC of Hacker et al. (2015), SiO<sub>2</sub>, Zr and Hf contents are lower in the Gangdese arc lower crust (Fig. 14B), which can be attributed to the lack of Zr–Hf–rich felsic rocks in the Late Cretaceous Gangdese arc lower crust. The Gangdese arc lower crust has higher Al<sub>2</sub>O<sub>3</sub> and Sr contents (Fig. 14B) than those of the LCC (Hacker et al.

2015; Rudnick and Gao 2014), indicating accumulation of plagioclase derived from low H<sub>2</sub>O primitive magma fractionation. The incompatible elements (Rb, Th, U, K, Pb, and LREE) in the Gangdese arc lower crust are 32–112% higher than the LCC of Rudnick and Gao (2014). The Gangdese arc lower crust has 9–72 % higher Rb, Th and U, and 9–26% lower K, Pb, and LREE contents than those of the LCC of Hacker et al. (2015) (Fig. 14B). The Cu content (71.3 ppm; Table S6) in the Gangdese lower crust is 2.7 times as high as the LCC (Rudnick and Gao 2014). The high Cu content is related to the high sulfide mode in the cumulate rocks from the Gangdese arc lower crust. The release of Cu from the lower crust into the post-collisional magma probably played an important role in the formation of the post-collisional porphyry copper deposits in the Gangdese belt (Hou et al. 2004). Except for Cu, the other transition metals (Mn, Sc, V, Cr, Co, Ni, and Zn) in the Gangdese arc lower crust are generally within <60% deviation with respect to the LCC of Rudnick and Gao (2014).

#### **Comparison with the other continental arc lower crust**

Several Phanerozoic continental arc crustal sections have been recognized worldwide (Ducea et al. 2015; Miller et al. 2009), but few expose the complete lower crust. The Southern Sierra Nevada section is one of the classic crustal sections of continental arc (Saleeby et al. 2003). Studies of exposed high-pressure rocks of the southern Sierra Nevada batholith and xenolith suites in Miocene volcanic rocks have revealed that the lower crust of the Sierra Nevada arc was mainly composed of mafic garnet granulites and gabbroic intrusions (Ducea and Saleeby 1998; Saleeby et al. 2003, 2007). The Fiordland in New Zealand exposes the deepest continental arc crustal section with paleodepths ranging from ~8 km to ~65 km (Clarke et al. 2013; De Paoli et al. 2009). The Mesozoic Fiordland arc lower crust is dominated by the gabbroic to dioritic granulites and minor eclogite (Chapman 2017; Dunkley 2010; Watton 2009; Wiesenfeld 2016). The Ordovician Famatinian arc in central Argentina is a continuous, tilted continental arc crustal section ranging depth from ~12 to ~30 km (Otamendi et al. 2012; Tibaldi et al. 2013). The

exposed Famatinian arc lower crust is dominated by mafic rocks with minor ultramafic rocks (Walker et al. 2015). The garnet granulites in some arc sections have been considered as the residues of partial melting of mafic rocks (Ducea et al. 2015; Stowell et al. 2014). However, recent studies have demonstrated that the compositional stratification of the arc crust, to first order, was controlled by fractional crystallization of arc magma, and that the gabbroic rocks or garnet granulites were cumulates derived from middle- to high-pressure fractional crystallization of arc magma (Chapman et al. 2016; Clarke et al. 2013; Jagoutz and Klein 2018; Lee et al. 2006; Walker et al. 2015; Wiesenfeld 2016). Geochronological data reveal that these continental arc lower crust sections were built through high-flux magmatic events within <15 Myr (Decker et al. 2017; Ducea et al. 2017; Saleeby et al. 2007; Schwartz et al. 2017). These characteristics of the continental arc crust sections are similar to those of the Gangdese arc.

We calculated the average compositions of the Famatinian and Fiordland arc lower crust. The lower half of the Famatinian arc crust includes ~5 km mafic unit and ~9 km intermediate unit based on the reconstruction through thermobarometry (Tibaldi et al. 2013). The result reveals that the Famatinian arc lower crust is basaltic andesite with SiO<sub>2</sub> of ~54 wt% and Mg# of ~53. The Fiordland arc lower crust (65–35 km paleodepth), represented by the average composition of the Breaksea Orthogneiss and Malaspina Pluton (Chapman 2017; Dunkley 2010; Watton 2009; Wiesenfeld 2016), is basaltic with SiO<sub>2</sub> of ~53 wt% and Mg# of ~53. Both the Famatinian and Fiordland arc lower crusts are enriched in highly incompatible elements (Fig. 14B), which is similar to the trace-element composition of the Gangdese arc lower crust. Although inferred crustal thickness between Gangdese, Famatinian, and Fiordland arc is different, their lower crust compositions are strikingly comparable with those of the average composition of LCC (Rudnick and Gao 2014). Based on the above observations, we consider that the continental arc lower crust is basaltic or basaltic andesite in composition and are characterized by enrichment in highly incompatible elements (Fig. 14B).

### Implications for continental crust formation

Arc magmas generated above subduction zones display geochemical compositions that are similar to the continental crust, indicating that the arc magmatism plays a significant role in creating continental crust (Taylor and McLennan 1995). Oceanic arc lower crust has systematically lower highly incompatible element concentrations than the estimates of the LCC (Jagoutz and Schmidt 2012; Kelemen and Behn 2016). Crustal relamination has been considered as an important process in refining the intra-oceanic arc lower crust into continental lower crust (Hacker et al. 2015; Kelemen and Behn 2016). Compared with the oceanic arc lower crust, the continental arc lower crust has higher highly incompatible elements, which is comparable with those of the LCC (Fig. 14B). This geochemical signature of the continental arc lower crust could be caused by the assimilation of continental basement or crustal relamination. Crustal assimilation is inevitable when the continental arc magma ascent through the crustal basement. For the Gangdese arc, no field evidence supports for significant crustal assimilation. The consistent and depleted Sr–Nd–Hf isotopic characteristics (Fig. 8) indicate that the Late Cretaceous Gangdese arc lower crust represents a significant addition of juvenile crust from depleted mantle without contribution from ancient crustal component. The Sr–Nd isotopic compositions of the mafic complex also indicate that crustal assimilation was limited in the Famatinian arc lower crust (Walker et al. 2015). Therefore, crustal assimilation plays only a minor role in contributing to the high concentration of the highly incompatible elements in the continental arc lower crust. According the model of relamination, about 50% felsic rocks are needed to match the pattern of incompatible trace elements of continental arc lower crust (Kelemen and Behn 2016), which would result in an obvious increase in SiO<sub>2</sub> of the lower crust. However, the continental arc lower crust sections are dominated by gabbroic rocks indicating that the crustal relamination, if present, was limited. The difference between the continental and oceanic arc lower crust is consistent with that the calc-alkaline primitive melts from

the continental arcs have higher incompatible element concentrations than those from the oceanic arcs (Schmidt and Jagoutz 2017). Therefore, the probable reason for the enrichment of highly incompatible elements in the continental arc lower crust is that its geochemical characteristics inherited from its primitive arc magma.

The geochemical and geophysical similarity between continental arc lower crust and LCC indicates that, after the detachment of high dense lower crust, no additional processes (such as relamination) are required to modify the continental arc lower crust into the LCC. The oceanic arc terrane can be transformed into a continental arc by accretion to adjacent continents. It is common that oceanic arc accretes onto the continental margin due to the geodynamic transition of the subducted oceanic lithosphere. For example, numerous accreted oceanic arcs have been identified in the Central Asian Orogenic Belt (Şengör et al. 2018) and along the western margins of the Americas (Saleeby 1983). Following accretion, continued subduction of oceanic lithosphere beneath the oceanic arc terrane give birth a new continental arc. Based on these observations, we consider that continental arc magmatism plays a critical role in continental crust formation.

## Conclusions

The Gangdese arc deep crust was built through the early (95–85 Ma) damp and late (86–78 Ma) wet fractional crystallization of arc magmas. The mafic-intermediate sequence in the Lilong Complex and the Kanniang Complex, which resulted from damp fractionation sequence of pyroxene → plagioclase → amphibole → biotite, formed the major part of the Gangdese arc lower crust. The minor ultramafic sequence in the Lilong Complex resulted from the wet fractionation sequence of olivine → pyroxene → amphibole → plagioclase. The 74–84 Ma Wolong granitoids were derived from fractional crystallization of wet arc magma and experienced crustal assimilation during emplacement. The Gangdese arc lower crust have consistent and depleted Sr–Nd–Hf isotopic compositions, indicating that it represents a significant addition of juvenile crust from depleted mantle. Calculated

seismic properties and geochemical composition of the Gangdese arc lower crust are comparable to those of the average lower continental crust. Unlike oceanic arc lower crust, which is depleted in highly incompatible elements and exhibits higher seismic wave speeds, the continental arc lower crust has similar highly incompatible elements concentrations and estimated seismic wave speeds with the lower continental crust. This indicates that continental arc magmatism is necessary in making the continental crust.

### Acknowledgements

We thank George Bergantz and Robert B. Miller for their constructive comments and Othmar Müntener for editorial comment and handling. This study is supported by the National Key Research and Development Project of China (2016YFC0600309), the Natural Science Foundation of China (41673036 and 41730211), the Open Research Program (GPMR201603) and MOST Special Fund (MSFGPMR201601–2) from State Key Laboratory of Geological Processes and Mineral Resources, the program from China Scholarship Council (No.201806415005). Wang-Chun Xu, Bi-Ji Luo, Fa-Bin Pan, He Yang, Lu Tao and De-Rong Qi are thanked for their help during the field work.

### References

- Abers GA, Hacker BR (2016) A MATLAB toolbox and Excel workbook for calculating the densities, seismic wave speeds, and major element composition of minerals and rocks at pressure and temperature. *Geochem Geophys Geosyst* 17:616-624. <https://doi.org/10.1002/2015gc006171>
- Alonso-Perez R, Müntener O, Ulmer P (2009) Igneous garnet and amphibole fractionation in the roots of island arcs: experimental constraints on andesitic liquids. *Contrib Mineral Petrol* 157:541.

<https://doi.org/10.1007/s00410-008-0351-8>

- Arndt NT, Goldstein SL (1989) An Open Boundary between Lower Continental-Crust and Mantle - Its Role in Crust Formation and Crustal Recycling. *Tectonophysics* 161:201-212. [https://doi.org/10.1016/0040-1951\(89\)90154-6](https://doi.org/10.1016/0040-1951(89)90154-6)
- Austrheim H (1998) Influence of Fluid and Deformation on Metamorphism of the Deep Crust and Consequences for the Geodynamics of Collision Zones. In: Hacker BR, Liou JG (ed) *When Continents Collide: Geodynamics and Geochemistry of Ultrahigh-Pressure Rocks*, vol. Springer Netherlands, Dordrecht, pp 297-323
- Beard JS, Lofgren GE (1991) Dehydration Melting and Water-Saturated Melting of Basaltic and Andesitic Greenstones and Amphibolites at 1, 3, and 6. 9 kb. *J Petrol* 32:365-401. <https://doi.org/10.1093/petrology/32.2.365>
- Calvert AJ (2011) The Seismic Structure of Island Arc Crust. In: *Arc-Continent Collision*, vol. Springer Berlin Heidelberg, Berlin, Heidelberg, pp 87-119
- Carmichael ISE (1991) The redox states of basic and silicic magmas: a reflection of their source regions? *Contrib Mineral Petrol* 106:129-141. <https://doi.org/10.1007/BF00306429>
- Chapman AD, Saleeby JB, Wood DJ, Piasecki A, Kidder S, Ducea MN, Farley KA (2012) Late Cretaceous gravitational collapse of the southern Sierra Nevada batholith, California. *Geosphere* 8:314-341. <https://doi.org/10.1130/GES00740.1>
- Chapman T (2017) *Deciphering Igneous and Metamorphic Histories from Exposed Deep Arc Crust, Fiordland, New Zealand: Crustal Differentiation and Evolution*. Dissertation. The University of Sydney
- Chapman T, Clarke GL, Daczko NR (2016) Crustal Differentiation in a Thickened Arc—Evaluating Depth Dependences. *J Petrol* 57:595-620. <https://doi.org/10.1093/petrology/egw022>
- Christensen NI, Mooney WD (1995) Seismic velocity structure and composition of the continental crust: A global

- view. *Journal of Geophysical Research: Solid Earth* 100:9761-9788. <https://doi.org/10.1029/95jb00259>
- Clarke GL, Daczko NR, Miescher D (2013) Identifying Relic Igneous Garnet and Clinopyroxene in Eclogite and Granulite, Breaksea Orthogneiss, New Zealand. *J Petrol* 54:1921-1938. <https://doi.org/10.1093/petrology/egt036>
- Clemens JD, Vielzeuf D (1987) Constraints on melting and magma production in the crust. *Earth Planet Sci Lett* 86:287-306. [https://doi.org/10.1016/0012-821X\(87\)90227-5](https://doi.org/10.1016/0012-821X(87)90227-5)
- Connolly JAD (2009) The geodynamic equation of state: What and how. *Geochem Geophys Geosyst* 10 <https://doi.org/10.1029/2009gc002540>
- Cottrell E, Kelley KA (2011) The oxidation state of Fe in MORB glasses and the oxygen fugacity of the upper mantle. *Earth Planet Sci Lett* 305:270-282. <https://doi.org/DOI:10.1016/j.epsl.2011.03.014>
- Davidson J, Turner S, Handley H, Macpherson C, Dosseto A (2007) Amphibole "sponge" in arc crust? *Geology* 35:787-790. <https://doi.org/10.1130/g23637a.1>
- De Paoli MC, Clarke GL, Klepeis KA, Allibone AH, Turnbull IM (2009) The Eclogite–Granulite Transition: Mafic and Intermediate Assemblages at Breaksea Sound, New Zealand. *J Petrol* 50:2307-2343. <https://doi.org/10.1093/petrology/egp078>
- Decker M, Schwartz JJ, Stowell HH, Klepeis KA, Tulloch AJ, Kitajima K, Valley JW, Kylander-Clark ARC (2017) Slab-Triggered Arc Flare-up in the Cretaceous Median Batholith and the Growth of Lower Arc Crust, Fiordland, New Zealand. *J Petrol* 58:1145-1171. <https://doi.org/10.1093/petrology/egx049>
- Dong X, Zhang Z, Santosh M (2010a) Zircon U-Pb Chronology of the Nyingtri Group, Southern Lhasa Terrane, Tibetan Plateau: Implications for Grenvillian and Pan-African Provenance and Mesozoic-Cenozoic Metamorphism. *The Journal of Geology* 118:677-690. <https://doi.org/10.1086/656355>
- Dong X, Zhang ZM, Geng GS, Liu F, Wang W, Yu F (2010b) Devonian magmatism from the southern Lhasa



terrane, Tibetan Plateau. *Acta Petrol Sin* 26:2226-2232.

Ducea M, Saleeby J (1998) Crustal recycling beneath continental arcs: silica-rich glass inclusions in ultramafic xenoliths from the Sierra Nevada, California. *Earth Planet Sci Lett* 156:101-116.

[https://doi.org/10.1016/S0012-821X\(98\)00021-1](https://doi.org/10.1016/S0012-821X(98)00021-1)

Ducea MN, Bergantz GW, Crowley JL, Otamendi J (2017) Ultrafast magmatic buildup and diversification to produce continental crust during subduction. *Geology* 45:235-238.

<https://doi.org/https://doi.org/10.1130/g38726.1>

Ducea MN, Saleeby JB, Bergantz G (2015) The Architecture, Chemistry, and Evolution of Continental Magmatic Arcs. *Annu Rev Earth Planet Sci* 43:299-331. <https://doi.org/10.1146/annurev-earth-060614-105049>

Dufek J, Bergantz GW (2005) Lower Crustal Magma Genesis and Preservation: a Stochastic Framework for the Evaluation of Basalt–Crust Interaction. *J Petrol* 46:2167-2195. <https://doi.org/10.1093/petrology/egi049>

Dunkley E (2010) Evolution of the Median Batholith, Fiordland, New Zealand. Dissertation. Macquarie University

Gao S, Rudnick RL, Yuan HL, Liu XM, Liu YS, Xu WL, Ling WL, Ayers J, Wang XC, Wang QH (2004) Recycling lower continental crust in the North China craton. *Nature* 432:892-897.

<https://doi.org/10.1038/nature03162>

Geng QR, Pan GT, Zheng LL, Chen ZL, Fisher RD, Sun ZM, Ou CS, Dong H, Wang XW, Li S, Lou XY, Fu H (2006) The Eastern Himalayan syntaxis: major tectonic domains, ophiolitic melanges and geologic evolution.

*J Asian Earth Sci* 27:265-285. <https://doi.org/10.1016/j.jseaes.2005.03.009>

Green ECR, White RW, Diener JFA, Powell R, Holland TJB, Palin RM (2016) Activity–composition relations for the calculation of partial melting equilibria in metabasic rocks. *J Metamorph Geol* 34:845-869.

<https://doi.org/10.1111/jmg.12211>

Guan Q, Zhu D-C, Zhao Z-D, Dong G-C, Zhang L-L, Li X-W, Liu M, Mo X-X, Liu Y-S, Yuan H-L (2012) Crustal

- thickening prior to 38 Ma in southern Tibet: Evidence from lower crust-derived adakitic magmatism in the Gangdese Batholith. *Gondwana Res* 21:88-99. <https://doi.org/10.1016/j.gr.2011.07.004>
- Guan Q, Zhu DC, Zhao ZD, Zhang LL, Liu M, Li XW, Yu F, Mo XX (2010) Late Cretaceous adakites in the eastern segment of the Gangdese Belt, southern Tibet: Products of Neo-Tethyan ridge subduction? *Acta Petrol Sin* 26:2165-2179.
- Guo L, Zhang H-F, Harris N, Luo B-J, Zhang W, Xu W-C (2019) Tectonic erosion and crustal relamination during the India-Asian continental collision: Insights from Eocene magmatism in the southeastern Gangdese belt. *Lithos* 346-347:105161. <https://doi.org/10.1016/j.lithos.2019.105161>
- Guo L, Zhang H-F, Harris N, Pan F-B, Xu W-C (2011) Origin and evolution of multi-stage felsic melts in eastern Gangdese belt: Constraints from U–Pb zircon dating and Hf isotopic composition. *Lithos* 127:54-67. <https://doi.org/10.1016/j.lithos.2011.08.005>
- Guo L, Zhang H-F, Harris N, Pan F-B, Xu W-C (2013) Late Cretaceous (~81 Ma) high-temperature metamorphism in the southeastern Lhasa terrane: Implication for the Neo-Tethys ocean ridge subduction. *Tectonophysics* 608:112-126. <https://doi.org/10.1016/j.tecto.2013.10.007>
- Guo L, Zhang H-F, Harris N, Parrish R, Xu W-C, Shi Z-L (2012) Paleogene crustal anatexis and metamorphism in Lhasa terrane, eastern Himalayan syntaxis: Evidence from U–Pb zircon ages and Hf isotopic compositions of the Nyingchi Complex. *Gondwana Res* 21:100-111. <https://doi.org/10.1016/j.gr.2011.03.002>
- Guo L, Zhang H-F, Harris N, Xu W-C, Pan F-B (2017) Detrital zircon U–Pb geochronology, trace-element and Hf isotope geochemistry of the metasedimentary rocks in the Eastern Himalayan syntaxis: Tectonic and paleogeographic implications. *Gondwana Res* 41:207-221. <https://doi.org/10.1016/j.gr.2015.07.013>
- Hacker BR, Kelemen PB, Behn MD (2011) Differentiation of the continental crust by relamination. *Earth Planet Sci Lett* 307:501-516. <https://doi.org/10.1016/j.epsl.2011.05.024>

Hacker BR, Kelemen PB, Behn MD (2015) Continental Lower Crust. *Annu Rev Earth Planet Sci* 43:167-205.

<https://doi.org/10.1146/annurev-earth-050212-124117>

Hawthorne FC, Oberti R, Harlow GE, Maresch WV, Martin RF, Schumacher JC, Welch MD (2012) Nomenclature

of the amphibole supergroup. *Am Mineral* 97:2031-2048. <https://doi.org/10.2138/am.2012.4276>

Holland T, Powell R (2003) Activity–composition relations for phases in petrological calculations: an asymmetric

multicomponent formulation. *Contrib Mineral Petrol* 145:492-501. <https://doi.org/10.1007/s00410-003-0464->

[z](#)

Holland TJB, Powell R (2011) An improved and extended internally consistent thermodynamic dataset for phases

of petrological interest, involving a new equation of state for solids. *J Metamorph Geol* 29:333-383.

<https://doi.org/DOI> 10.1111/j.1525-1314.2010.00923.x

Hou ZQ, Gao YF, Qu XM, Rui ZY, Mo XX (2004) Origin of adakitic intrusives generated during mid-Miocene

east–west extension in southern Tibet. *Earth Planet Sci Lett* 220:139-155. <https://doi.org/10.1016/S0012->

[821X\(04\)00007-X](#)

Hu ZC, Liu YS, Gao S, Liu WG, Zhang W, Tong XR, Lin L, Zong KQ, Li M, Chen HH, Zhou L, Yang L (2012)

Improved in situ Hf isotope ratio analysis of zircon using newly designed X skimmer cone and jet sample

cone in combination with the addition of nitrogen by laser ablation multiple collector ICP-MS. *J Anal At*

*Spectrom* 27:1391-1399. <https://doi.org/10.1039/C2ja30078h>

Jagoutz O (2010) Construction of the granitoid crust of an island arc. Part II: a quantitative petrogenetic model.

*Contrib Mineral Petrol* 160:359-381. <https://doi.org/10.1007/s00410-009-0482-6>

Jagoutz O, Behn MD (2013) Foundering of lower island-arc crust as an explanation for the origin of the continental

Moho. *Nature* 504:131-134. <https://doi.org/10.1038/nature12758>

Jagoutz O, Kelemen PB (2015) Role of arc processes in the formation of continental crust. *Annu Rev Earth Planet*

Sci 43:363-404. <https://doi.org/10.1146/annurev-earth-040809-152345>

Jagoutz O, Klein B (2018) On the importance of crystallization-differentiation for the generation of SiO<sub>2</sub>-rich melts and the compositional build-up of arc (and continental) crust. *Am J Sci* 318:29-63.

<https://doi.org/10.2475/01.2018.03>

Jagoutz O, Müntener O, Schmidt MW, Burg J-P (2011) The roles of flux- and decompression melting and their respective fractionation lines for continental crust formation: Evidence from the Kohistan arc. *Earth Planet Sci Lett* 303:25-36. <https://doi.org/10.1016/j.epsl.2010.12.017>

Jagoutz O, Schmidt M, Enggist A, Burg J-P, Hamid D, Hussain S (2013) TTG-type plutonic rocks formed in a modern arc batholith by hydrous fractionation in the lower arc crust. *Contrib Mineral Petrol* 166:1099-1118.

<https://doi.org/10.1007/s00410-013-0911-4>

Jagoutz O, Schmidt MW (2012) The formation and bulk composition of modern juvenile continental crust: The Kohistan arc. *Chem Geol* 298–299:79-96. <https://doi.org/10.1016/j.chemgeo.2011.10.022>

Ji W-Q, Wu F-Y, Chung S-L, Liu C-Z (2012) Identification of Early Carboniferous granitoids from southern Tibet and implications for terrane assembly related to the Paleo-Tethyan evolution. *The Journal of Geology* 120:531-541. <https://doi.org/10.1086/666742>

Ji W-Q, Wu F-Y, Chung S-L, Liu C-Z (2014) The Gangdese magmatic constraints on a latest Cretaceous lithospheric delamination of the Lhasa terrane, southern Tibet. *Lithos* 210–211:168-180.

<https://doi.org/10.1016/j.lithos.2014.10.001>

Ji WQ, Wu FY, Chung SL, Li JX, Liu CZ (2009) Zircon U-Pb geochronology and Hf isotopic constraints on petrogenesis of the Gangdese batholith, southern Tibet. *Chem Geol* 262:229-245.

<https://doi.org/10.1016/j.chemgeo.2009.01.020>

Kapp P, DeCelles PG, Leier AL, Fabijanic JM, He SD, Pullen A, Gehrels GE (2007) The Gangdese retroarc thrust

belt revealed. *GSA Today* 17:4-9.

Kapp P, Yin A, Harrison TM, Ding L (2005) Cretaceous-Tertiary shortening, basin development, and volcanism in central Tibet. *Geol Soc Am Bull* 117:865-878. <https://doi.org/10.1130/B25595.1>

Kay RW, Kay SM (1993) Delamination and Delamination Magmatism. *Tectonophysics* 219:177-189. [https://doi.org/10.1016/0040-1951\(93\)90295-U](https://doi.org/10.1016/0040-1951(93)90295-U)

Kelemen PB, Behn MD (2016) Formation of lower continental crust by relamination of buoyant arc lavas and plutons. *Nature Geosci* 9:197-205. <https://doi.org/10.1038/ngeo2662>

Kelley KA, Cottrell E (2012) The influence of magmatic differentiation on the oxidation state of Fe in a basaltic arc magma. *Earth Planet Sci Lett* 329-330:109-121. <https://doi.org/10.1016/j.epsl.2012.02.010>

Krawczynski MJ, Grove TL, Behrens H (2012) Amphibole stability in primitive arc magmas: effects of temperature, H<sub>2</sub>O content, and oxygen fugacity. *Contrib Mineral Petrol* 164:317-339. <https://doi.org/10.1007/s00410-012-0740-x>

Lee C-TA, Cheng X, Horodyskyj U (2006) The development and refinement of continental arcs by primary basaltic magmatism, garnet pyroxenite accumulation, basaltic recharge and delamination: insights from the Sierra Nevada, California. *Contrib Mineral Petrol* 151:222-242. <https://doi.org/10.1007/s00410-005-0056-1>

Lin YH, Zhang ZM, Dong X, Shen K, Lu X (2013) Precambrian evolution of the Lhasa terrane, Tibet: Constraint from the zircon U–Pb geochronology of the gneisses. *Precambrian Res* 237:64-77. <https://doi.org/10.1016/j.precamres.2013.09.006>

Liu YS, Gao S, Hu ZC, Gao CG, Zong KQ, Wang DB (2010) Continental and Oceanic Crust Recycling-induced Melt-Peridotite Interactions in the Trans-North China Orogen: U-Pb Dating, Hf Isotopes and Trace Elements in Zircons from Mantle Xenoliths. *J Petrol* 51:537-571. <https://doi.org/10.1093/petrology/egp082>

Ludwig KR (2003) User's manual for isoplot 3.00, a geochronological toolkit for microsoft excel. Berkeley

Geochronol Cent Spec Publ 4:25-32.

Ma L, Wang Q, Li ZX, Wyman DA, Jiang ZQ, Yang JH, Gou GN, Guo HF (2013a) Early Late Cretaceous (ca. 93 Ma) norites and hornblendites in the Milin area, eastern Gangdese: Lithosphere–asthenosphere interaction during slab roll-back and an insight into early Late Cretaceous (ca. 100–80 Ma) magmatic “flare-up” in southern Lhasa (Tibet). *Lithos* 172–173:17-30. <https://doi.org/10.1016/j.lithos.2013.03.007>

Ma L, Wang Q, Wyman DA, Li ZX, Jiang ZQ, Yang JH, Gou GN, Guo HF (2013b) Late Cretaceous (100–89 Ma) magnesian charnockites with adakitic affinities in the Milin area, eastern Gangdese: Partial melting of subducted oceanic crust and implications for crustal growth in southern Tibet. *Lithos* 175–176:315-332. <https://doi.org/10.1016/j.lithos.2013.04.006>

McDonough WF, Sun Ss (1995) The composition of the Earth. *Chem Geol* 120:223-253. [https://doi.org/10.1016/0009-2541\(94\)00140-4](https://doi.org/10.1016/0009-2541(94)00140-4)

Miller RB, Paterson SR, Matzel JP, Miller RB, Snoke AW (2009) Plutonism at different crustal levels: Insights from the ~5–40 km (paleodepth) North Cascades crustal section, Washington. In: *Crustal Cross Sections from the Western North American Cordillera and Elsewhere: Implications for Tectonic and Petrologic Processes*, vol 456. Geological Society of America, pp 1-38

Mitchell AL, Gaetani GA, O’Leary JA, Hauri EH (2017) H<sub>2</sub>O solubility in basalt at upper mantle conditions. *Contrib Mineral Petrol* 172:85. <https://doi.org/10.1007/s00410-017-1401-x>

Müntener O, Kelemen PB, Grove TL (2001) The role of H<sub>2</sub>O during crystallization of primitive arc magmas under uppermost mantle conditions and genesis of igneous pyroxenites: an experimental study. *Contrib Mineral Petrol* 141:643-658. <https://doi.org/10.1007/s004100100266>

Müntener O, Ulmer P (2018) Arc crust formation and differentiation constrained by experimental petrology. *Am J Sci* 318:64-89. <https://doi.org/10.2475/01.2018.04>

- Murphy MA, Yin A, Harrison TM, Durr SB, Chen Z, Ryerson FJ, Kidd WSF, Wang X, Zhou X (1997) Did the Indo-Asian collision alone create the Tibetan plateau? *Geology* 25:719-722. [https://doi.org/10.1130/0091-7613\(1997\)025<0719:DTIACA>2.3.CO;2](https://doi.org/10.1130/0091-7613(1997)025<0719:DTIACA>2.3.CO;2)
- Nandedkar RH, Ulmer P, Müntener O (2014) Fractional crystallization of primitive, hydrous arc magmas: an experimental study at 0.7 GPa. *Contrib Mineral Petrol* 167:1015. <https://doi.org/10.1007/s00410-014-1015-5>
- Otamendi JE, Cristofolini E, Tibaldi AM, Quevedo FI, Baliani I (2010) Petrology of mafic and ultramafic layered rocks from the Jaboncillo Valley, Sierra de Valle Fértil, Argentina: Implications for the evolution of magmas in the lower crust of the Famatinian arc. *J South Am Earth Sci* 29:685-704. <https://doi.org/10.1016/j.jsames.2009.11.001>
- Otamendi JE, Ducea MN, Bergantz GW (2012) Geological, Petrological and Geochemical Evidence for Progressive Construction of an Arc Crustal Section, Sierra de Valle Fértil, Famatinian Arc, Argentina. *J Petrol* 53:761-800. <https://doi.org/10.1093/petrology/egr079>
- Otamendi JE, Ducea MN, Tibaldi AM, Bergantz GW, de la Rosa JD, Vujovich GI (2009a) Generation of Tonalitic and Dioritic Magmas by Coupled Partial Melting of Gabbroic and Metasedimentary Rocks within the Deep Crust of the Famatinian Magmatic Arc, Argentina. *J Petrol* 50:841-873. <https://doi.org/10.1093/petrology/egp022>
- Otamendi JE, Tiepolo M, Walker BA, Cristofolini EA, Tibaldi AM (2016) Trace elements in minerals from mafic and ultramafic cumulates of the central Sierra de Valle Fértil, Famatinian arc, Argentina. *Lithos* 240-243:355-370. <https://doi.org/10.1016/j.lithos.2015.11.009>
- Otamendi JE, Vujovich GI, de la Rosa JD, Tibaldi AM, Castro A, Martino RD, Pinotti LP (2009b) Geology and petrology of a deep crustal zone from the Famatinian paleo-arc, Sierras de Valle Fértil and La Huerta, San Juan, Argentina. *J South Am Earth Sci* 27:258-279. <https://doi.org/10.1016/j.jsames.2008.11.007>

- Pan GT, Mo XX, Hou ZQ, Zhu DC, Wang LQ, Li GM, Zhao ZD, Geng QR, Liao ZL (2006) Spatial-temporal framework of the Gangdese Orogenic Belt and its evolution. *Acta Petrol Sin* 22:521-533.
- Rapp RP, Watson EB (1995) Dehydration melting of metabasalt at 8-32-Kbar: Implications for continental growth and crust-mantle recycling. *J Petrol* 36:891-931. <https://doi.org/10.1093/petrology/36.4.891>
- Rapp RP, Watson EB, Miller CF (1991) Partial melting of amphibolite/eclogite and the origin of Archean trondhjemites and tonalites. *Precambrian Res* 51:1-25. [https://doi.org/10.1016/0301-9268\(91\)90092-o](https://doi.org/10.1016/0301-9268(91)90092-o)
- Rudnick RL, Gao S (2014) Composition of the continental crust. In: Holland H, Turekian K (ed) *Treatise on Geochemistry (Second Edition)*, vol. Elsevier, Oxford, pp 1-51
- Saleeby J, Ducea M, Clemens-Knott D (2003) Production and loss of high-density batholithic root, southern Sierra Nevada, California. *Tectonics* 22 <https://doi.org/10.1029/2002tc001374>
- Saleeby J, Farley KA, Kistler RW, Fleck RJ, Cloos M, Carlson WD, Gilbert MC, Liou JG, Sorensen SS (2007) Thermal evolution and exhumation of deep-level batholithic exposures, southernmost Sierra Nevada, California. In: *Convergent Margin Terranes and Associated Regions: A Tribute to WG Ernst*, vol 419. Geological Society of America, pp 39-66
- Saleeby JB (1983) Accretionary tectonics of the north American Cordillera. *Annu Rev Earth Planet Sci* 11:45-73. <https://doi.org/10.1146/annurev.ea.11.050183.000401>
- Schmidt MW (1992) Amphibole composition in tonalite as a function of pressure: an experimental calibration of the Al-in-hornblende barometer. *Contrib Mineral Petrol* 110:304-310. <https://doi.org/10.1007/bf00310745>
- Schmidt MW, Jagoutz O (2017) The global systematics of primitive arc melts. *Geochem Geophys Geosyst* 18:2817-2854. <https://doi.org/10.1002/2016gc006699>
- Schmidt MW, Poli S (2004) Magmatic Epidote. *Rev Mineral Geochem* 56:399-430. <https://doi.org/10.2138/gsrmg.56.1.399>



- Schwartz JJ, Klepeis KA, Sadorski JF, Stowell HH, Tulloch AJ, Coble MA (2017) The tempo of continental arc construction in the Mesozoic Median Batholith, Fiordland, New Zealand. *Lithosphere* 9:343-365. <https://doi.org/10.1130/1610.1>
- Şengör AMC, Natal'in BA, Sunal G, van der Voo R (2018) The Tectonics of the Altaids: Crustal Growth During the Construction of the Continental Lithosphere of Central Asia Between ~750 and ~130 Ma Ago. *Annu Rev Earth Planet Sci* 46:439-494. <https://doi.org/10.1146/annurev-earth-060313-054826>
- Sisson TW, Grove TL (1993) Experimental investigations of the role of H<sub>2</sub>O in calc-alkaline differentiation and subduction zone magmatism. *Contrib Mineral Petrol* 113:143-166. <https://doi.org/10.1007/bf00283225>
- Stowell H, Parker KO, Gatewood M, Tulloch A, Koenig A (2014) Temporal links between pluton emplacement, garnet granulite metamorphism, partial melting and extensional collapse in the lower crust of a Cretaceous magmatic arc, Fiordland, New Zealand. *J Metamorph Geol* 32:151-175. <https://doi.org/10.1111/jmg.12064>
- Tang Y-W, Chen L, Zhao Z-F, Zheng Y-F (2019) Geochemical evidence for the production of granitoids through reworking of the juvenile mafic arc crust in the Gangdese orogen, southern Tibet. *GSA Bulletin* <https://doi.org/10.1130/b35304.1>
- Taylor SR, McLennan SM (1995) The geochemical evolution of the continental crust. *Rev Geophys* 33:241-265. <https://doi.org/10.1029/95rg00262>
- Tibaldi AM, Otamendi JE, Cristofolini EA, Baliani I, Walker BA, Bergantz GW (2013) Reconstruction of the Early Ordovician Famatinian arc through thermobarometry in lower and middle crustal exposures, Sierra de Valle Fértil, Argentina. *Tectonophysics* 589:151-166. <https://doi.org/10.1016/j.tecto.2012.12.032>
- Ulmer P, Kaegi R, Müntener O (2018) Experimentally Derived Intermediate to Silica-rich Arc Magmas by Fractional and Equilibrium Crystallization at 1·0 GPa: an Evaluation of Phase Relationships, Compositions, Liquid Lines of Descent and Oxygen Fugacity. *J Petrol* 59:11-58. <https://doi.org/10.1093/petrology/egy017>

- Walker BA, Jr, Bergantz GW, Otamendi JE, Ducea MN, Cristofolini EA (2015) A MASH Zone Revealed: the Mafic Complex of the Sierra Valle Fértil. *J Petrol* 56:1863-1896. <https://doi.org/10.1093/petrology/egv057>
- Wang J, Li X, Ning W, Kusky T, Wang L, Polat A, Deng H (2019) Geology of a Neoproterozoic suture: Evidence from the Zunhua ophiolitic mélangé of the Eastern Hebei Province, North China Craton. *GSA Bulletin* 131:1943-1964. <https://doi.org/10.1130/b35138.1>
- Watton JW (2009) Petrographic and geochemical characterisation of the Breaksea Orthogneiss, Fiordland, New Zealand. Dissertation. Macquarie University
- Wen DR, Chung SL, Song B, Iizuka Y, Yang HJ, Ji JQ, Liu DY, Gallet S (2008) Late Cretaceous Gangdese intrusions of adakitic geochemical characteristics, SE Tibet: Petrogenesis and tectonic implications. *Lithos* 105:1-11. <https://doi.org/10.1016/j.lithos.2008.02.005>
- White, Powell, Holland, Worley (2000) The effect of TiO<sub>2</sub> and Fe<sub>2</sub>O<sub>3</sub> on metapelitic assemblages at greenschist and amphibolite facies conditions: mineral equilibria calculations in the system K<sub>2</sub>O–FeO–MgO–Al<sub>2</sub>O<sub>3</sub>–SiO<sub>2</sub>–H<sub>2</sub>O–TiO<sub>2</sub>–Fe<sub>2</sub>O<sub>3</sub>. *J Metamorph Geol* 18:497-511. <https://doi.org/10.1046/j.1525-1314.2000.00269.x>
- White RW, Powell R, Clarke GL (2002) The interpretation of reaction textures in Fe-rich metapelitic granulites of the Musgrave Block, central Australia: constraints from mineral equilibria calculations in the system K<sub>2</sub>O–FeO–MgO–Al<sub>2</sub>O<sub>3</sub>–SiO<sub>2</sub>–H<sub>2</sub>O–TiO<sub>2</sub>–Fe<sub>2</sub>O<sub>3</sub>. *J Metamorph Geol* 20:41-55. <https://doi.org/10.1046/j.0263-4929.2001.00349.x>
- White RW, Powell R, Holland TJB, Johnson TE, Green ECR (2014a) New mineral activity–composition relations for thermodynamic calculations in metapelitic systems. *J Metamorph Geol* 32:261-286. <https://doi.org/10.1111/jmg.12071>
- White RW, Powell R, Johnson TE (2014b) The effect of Mn on mineral stability in metapelites revisited: new a–x relations for manganese-bearing minerals. *J Metamorph Geol* 32:809-828.

<https://doi.org/10.1111/jmg.12095>

Wiesefeld J (2016) Construction of continental crust by deep crustal fractional crystallization and garnet pyroxenite root development: geochemical evidence from Fiordland, New Zealand. Dissertation. California State University, Northridge

Xu W, Zhu D-C, Wang Q, Weinberg RF, Wang R, Li S-M, Zhang L-L, Zhao Z-D (2019) Constructing the Early Mesozoic Gangdese Crust in Southern Tibet by Hornblende-dominated Magmatic Differentiation. *J Petrol* 60:515-552. <https://doi.org/10.1093/petrology/egz005>

Xu Z, Ji S, Cai Z, Zeng L, Geng Q, Cao H (2012) Kinematics and dynamics of the Namche Barwa Syntaxis, eastern Himalaya: Constraints from deformation, fabrics and geochronology. *Gondwana Res* 21:19-36. <https://doi.org/10.1016/j.gr.2011.06.010>

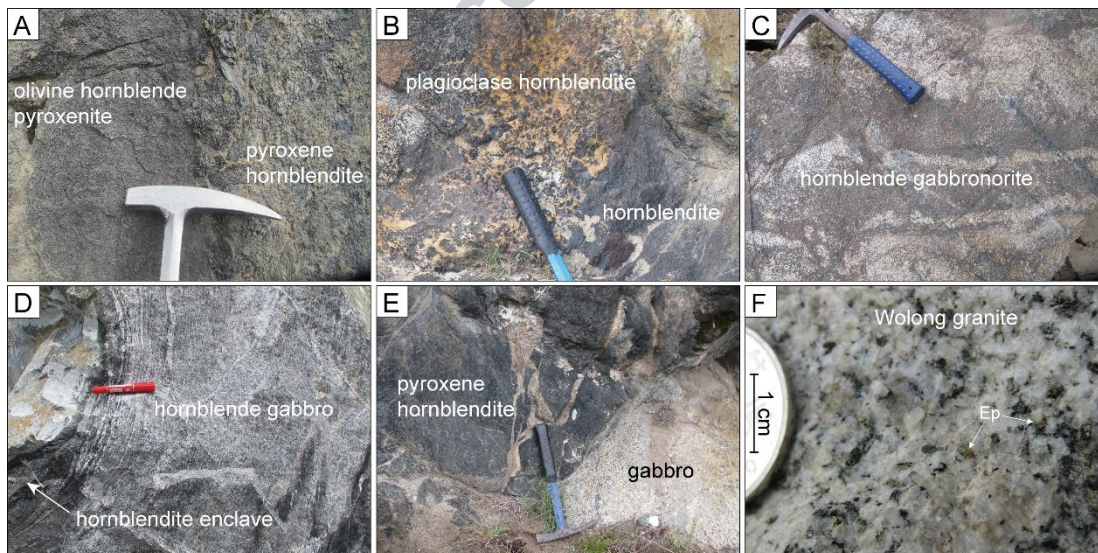
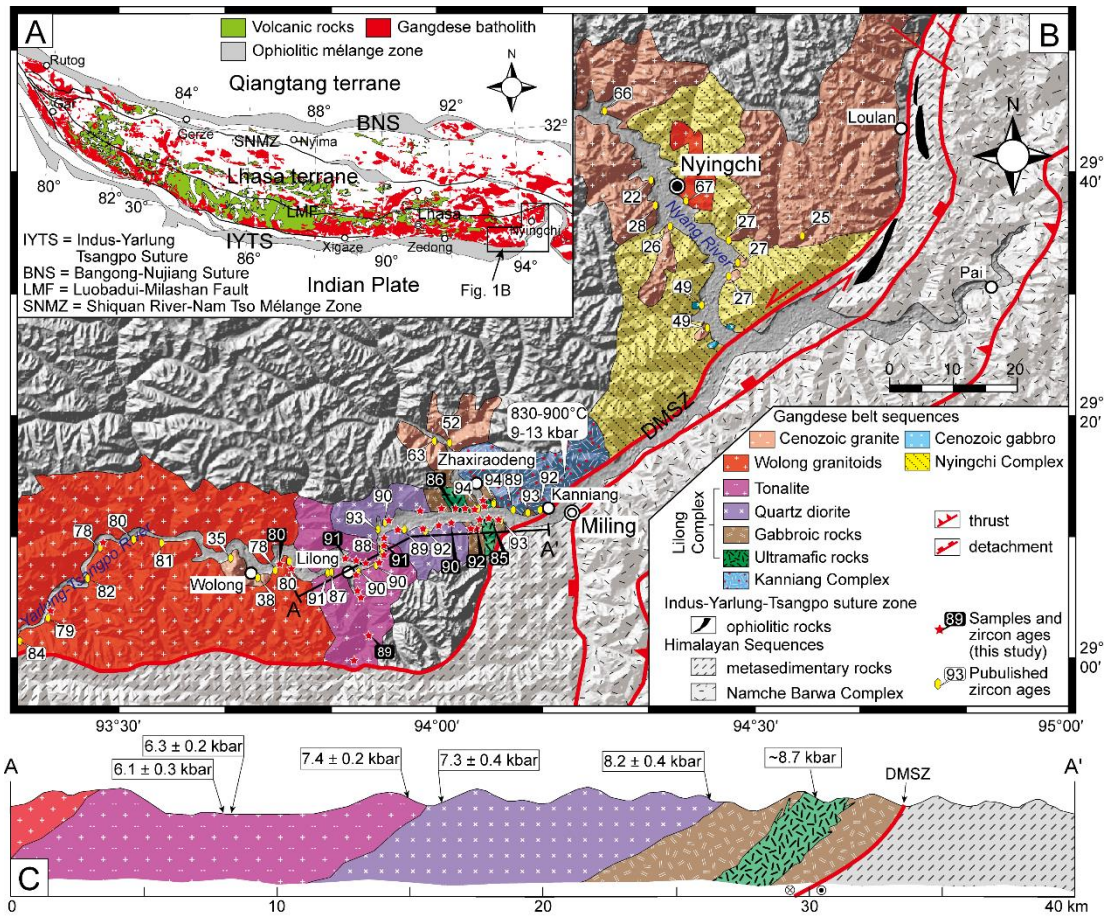
Yin A, Harrison TM (2000) Geologic evolution of the Himalayan-Tibetan orogen. *Annu Rev Earth Planet Sci* 28:211-280. <https://doi.org/10.1146/annurev.earth.28.1.211>

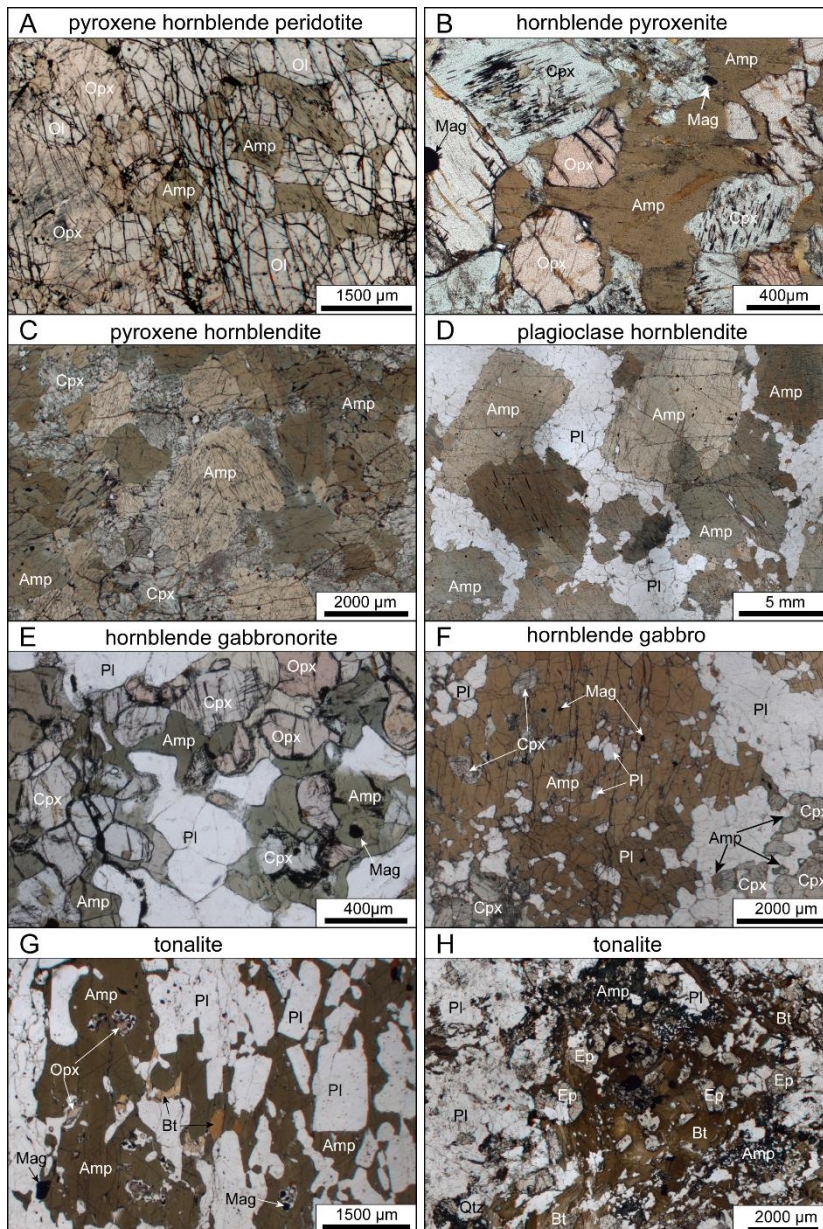
Zeitler PK, Meltzer AS, Brown L, Kidd WSF, Lim C, Enkelmann E, Nie J, Horton BK, Hoke GD (2014) Tectonics and topographic evolution of Namche Barwa and the easternmost Lhasa block, Tibet. In: *Toward an Improved Understanding of Uplift Mechanisms and the Elevation History of the Tibetan Plateau*, vol 507. Geological Society of America, p 0

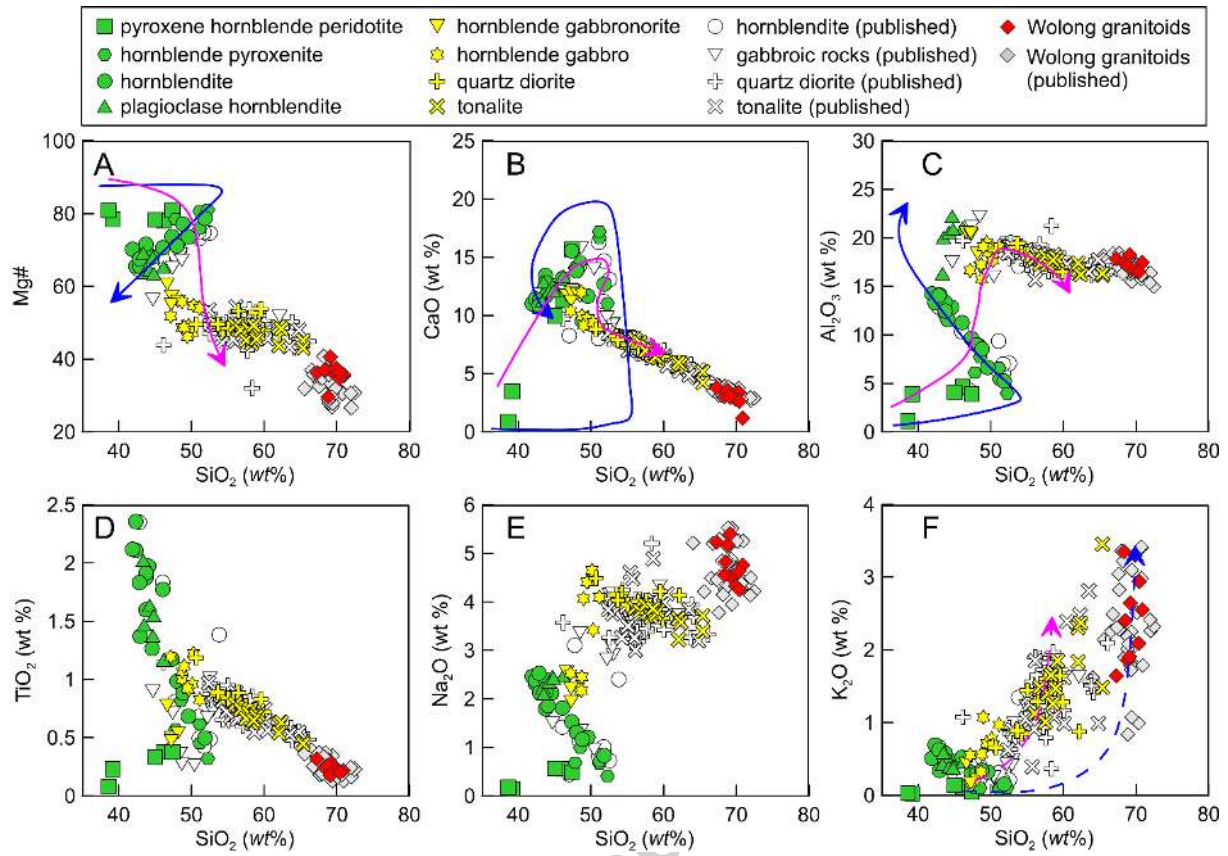
Zhang HF, Harris N, Guo L, Xu WC (2010a) The significance of Cenozoic magmatism from the western margin of the eastern syntaxis, southeast Tibet. *Contrib Mineral Petrol* 160:83-98. <https://doi.org/10.1007/s00410-009-0467-5>

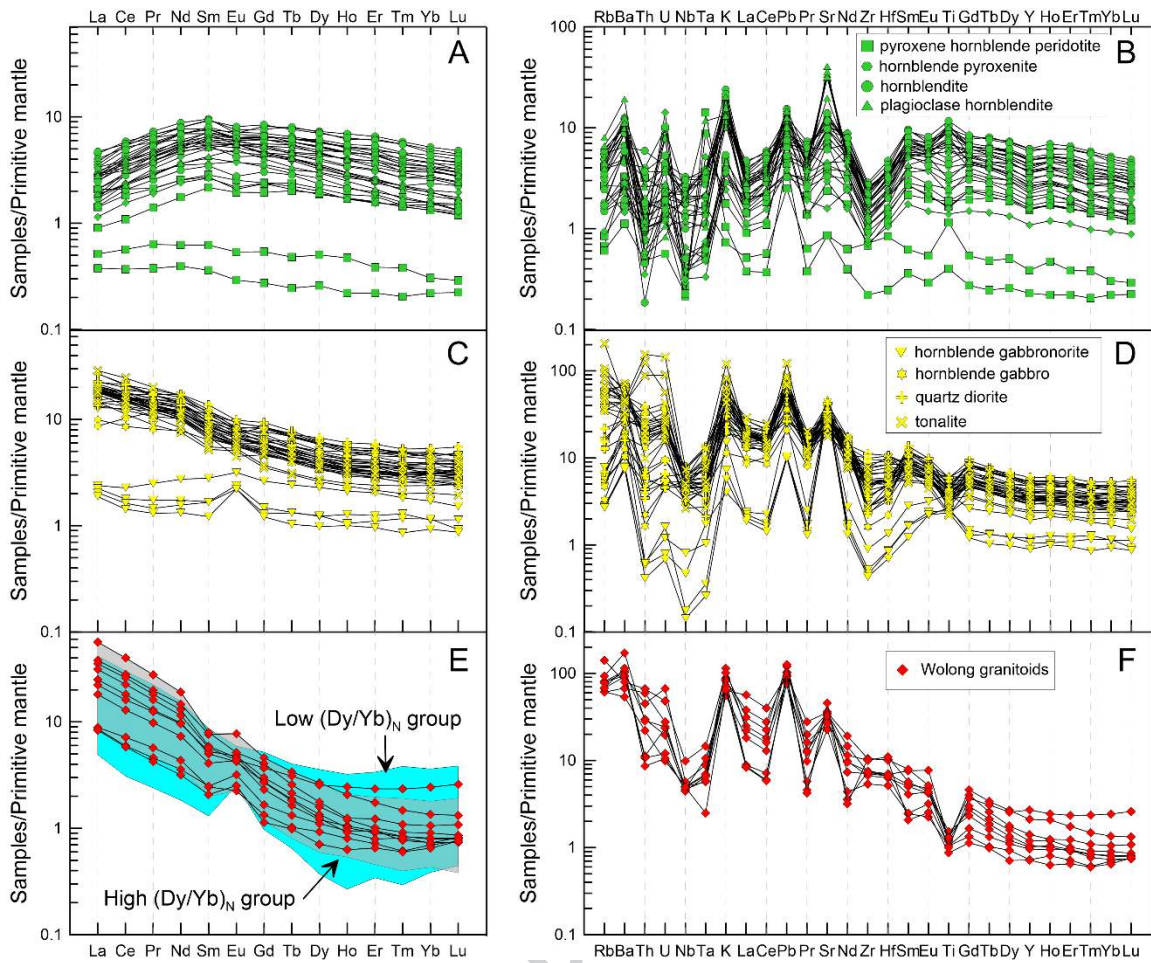
Zhang HF, Xu WC, Zong KQ, Yuan HL, Harris N (2008) Tectonic evolution of metasediments from the Gangdise terrane, Asian plate, Eastern Himalayan Syntaxis, Tibet. *Int Geol Rev* 50:914-930. <https://doi.org/10.2747/0020-6814.50.10.914>

- Zhang Z, Ding H, Palin RM, Dong X, Tian Z, Chen Y (2020) The lower crust of the Gangdese magmatic arc, southern Tibet, implication for the growth of continental crust. *Gondwana Res* 77:136-146.  
<https://doi.org/10.1016/j.gr.2019.07.010>
- Zhang Z, Zhao G, Santosh M, Wang J, Dong X, Shen K (2010b) Late Cretaceous charnockite with adakitic affinities from the Gangdese batholith, southeastern Tibet: Evidence for Neo-Tethyan mid-ocean ridge subduction? *Gondwana Res* 17:615-631. <https://doi.org/10.1016/j.gr.2009.10.007>
- Zhang ZM, Dong X, Xiang H, He ZY, Liou JG (2014) Metagabbros of the Gangdese arc root, south Tibet: Implications for the growth of continental crust. *Geochim Cosmochim Acta* 143:268-284.  
<https://doi.org/10.1016/j.gca.2014.01.045>
- Zhang ZM, Dong X, Xiang H, Liou JG, Santosh M (2013) Building of the Deep Gangdese Arc, South Tibet: Paleocene Plutonism and Granulite-Facies Metamorphism. *J Petrol* 54:2547-2580.  
<https://doi.org/10.1093/petrology/egt056>
- Zhang ZM, Zhao GC, Santosh M, Wang JL, Dong X, Liou JG (2010c) Two stages of granulite facies metamorphism in the eastern Himalayan syntaxis, south Tibet: petrology, zircon geochronology and implications for the subduction of Neo-Tethys and the Indian continent beneath Asia. *J Metamorph Geol* 28:719-733. <https://doi.org/10.1111/j.1525-1314.2010.00885.x>
- Zhu DC, Zhao ZD, Niu YL, Mo XX, Chung SL, Hou ZQ, Wang LQ, Wu FY (2011) The Lhasa Terrane: Record of a microcontinent and its histories of drift and growth. *Earth Planet Sci Lett* 301:241-255.  
<https://doi.org/10.1016/j.epsl.2010.11.005>

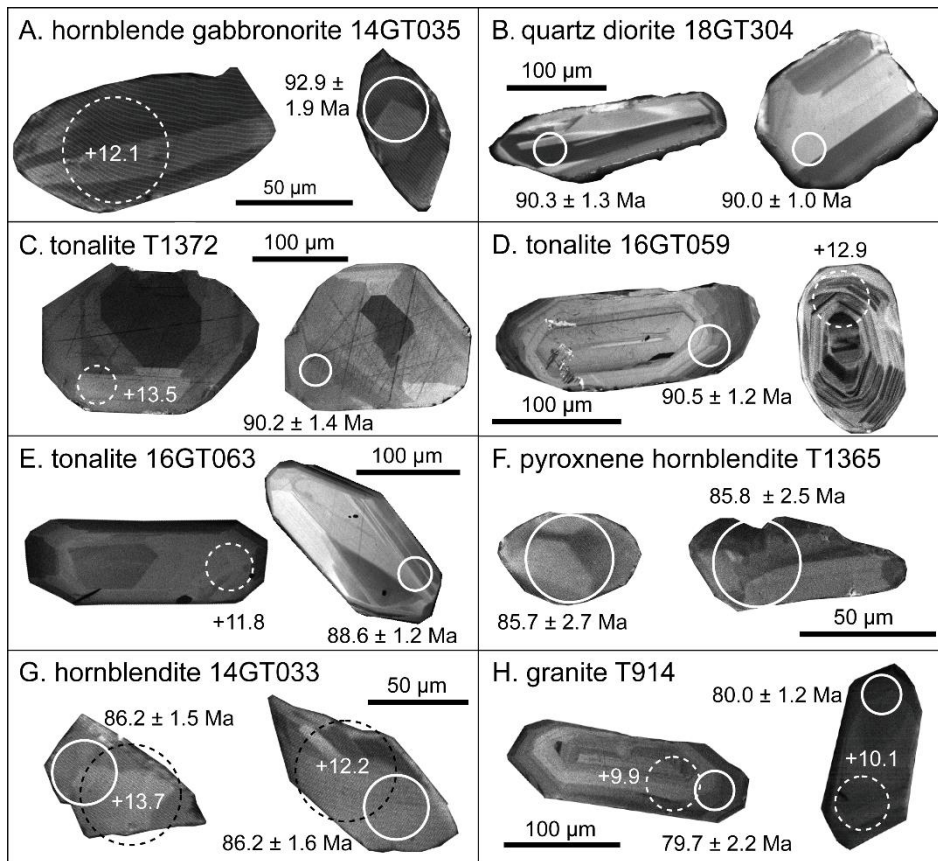


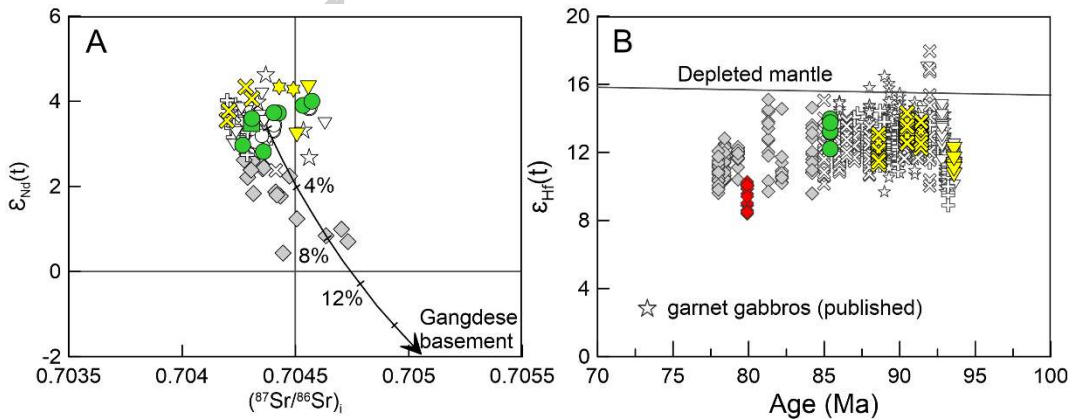
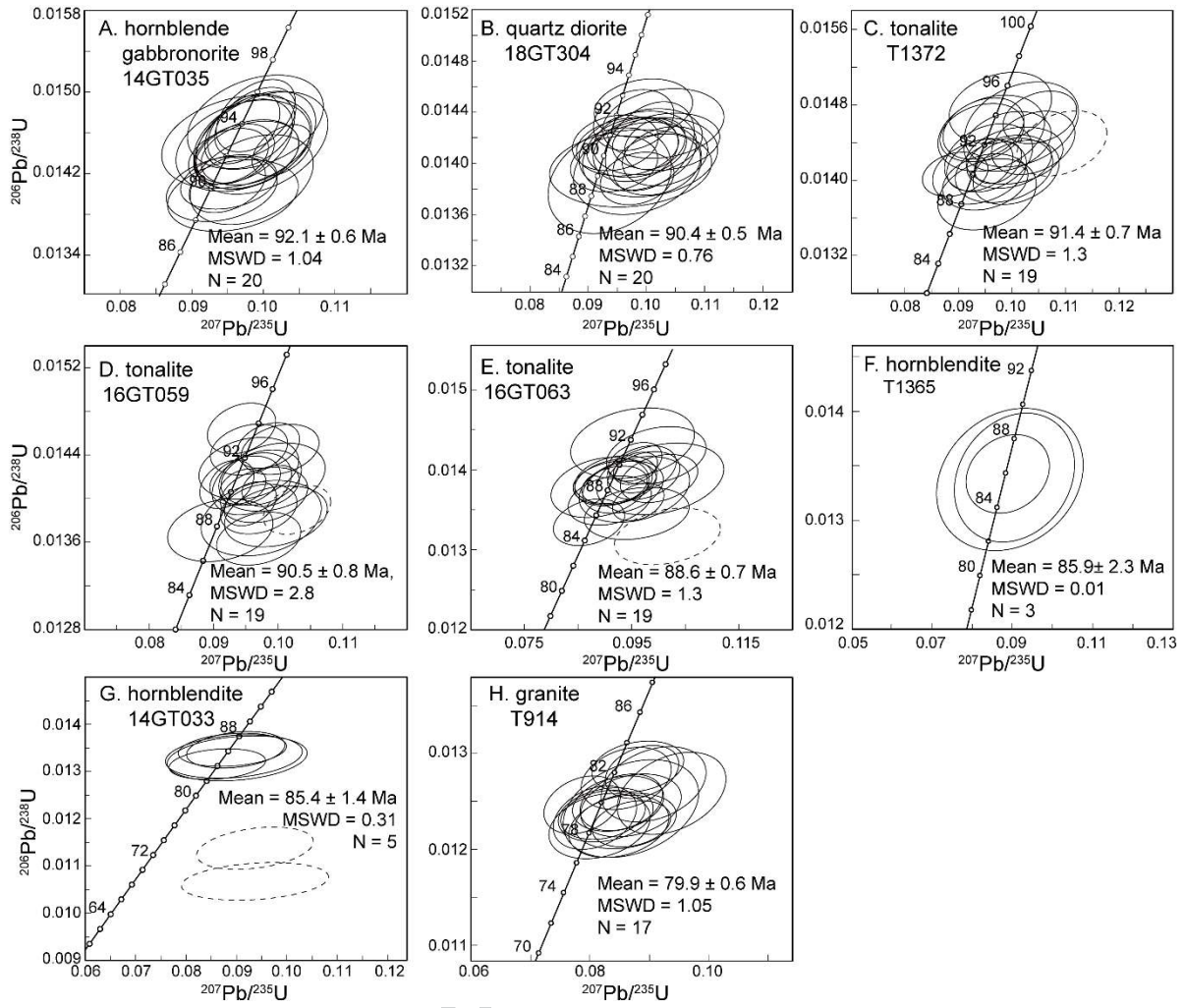


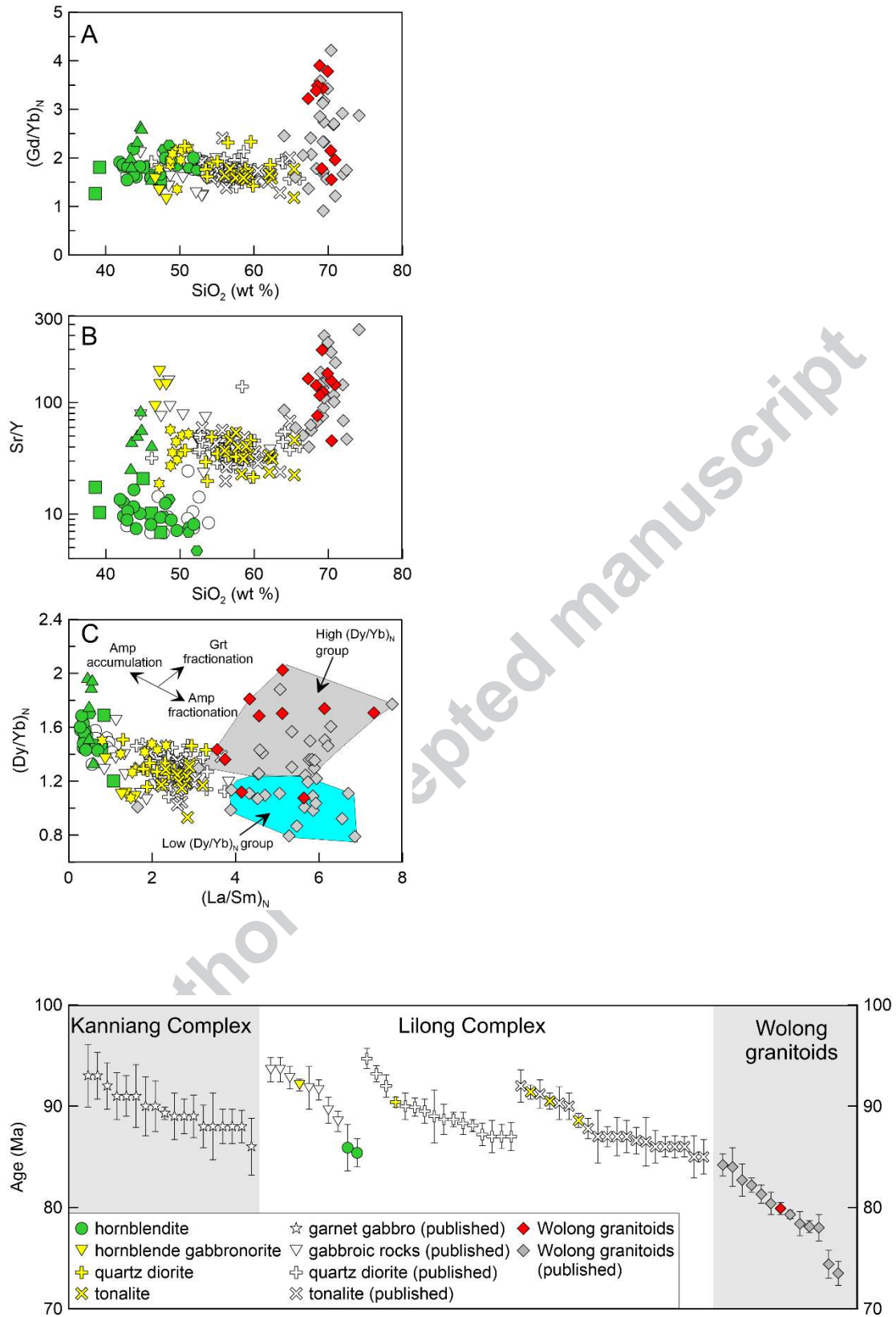


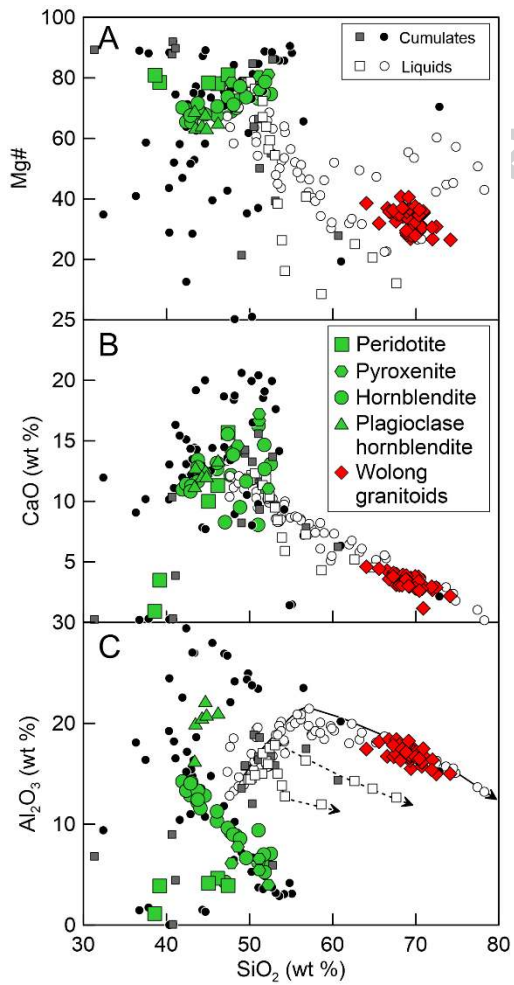
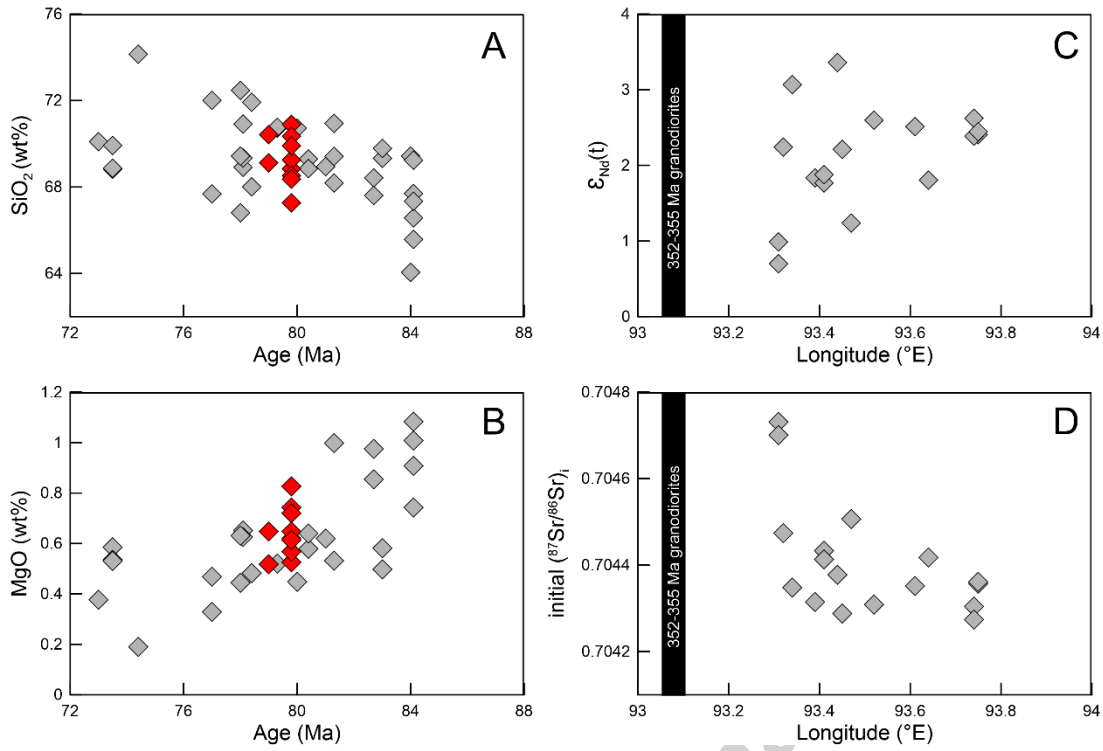












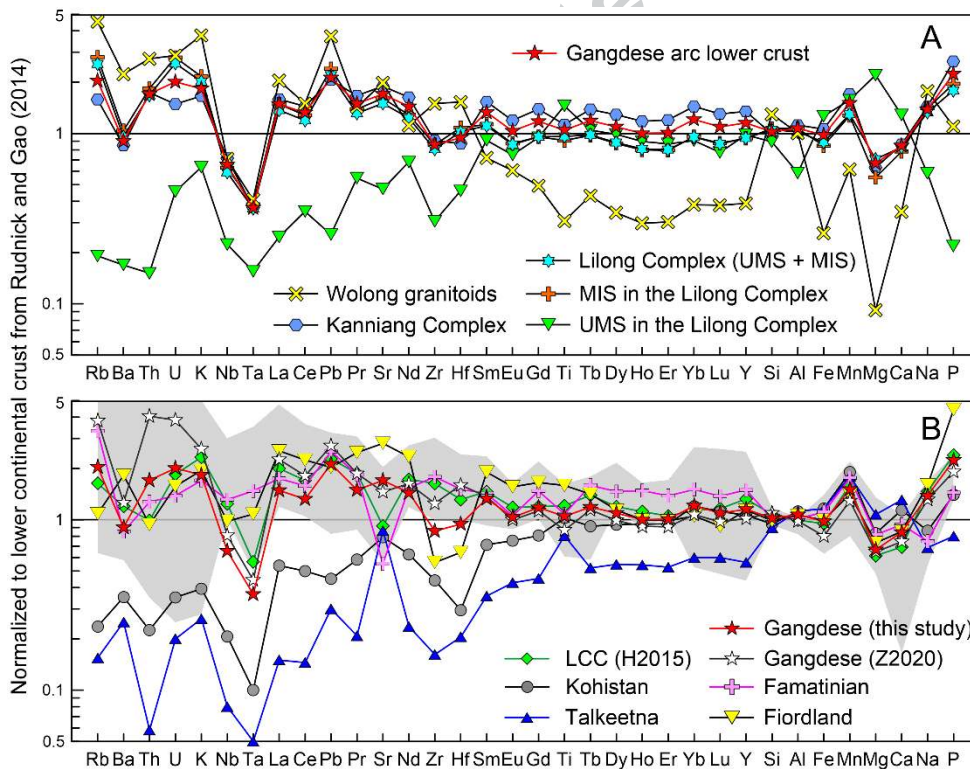
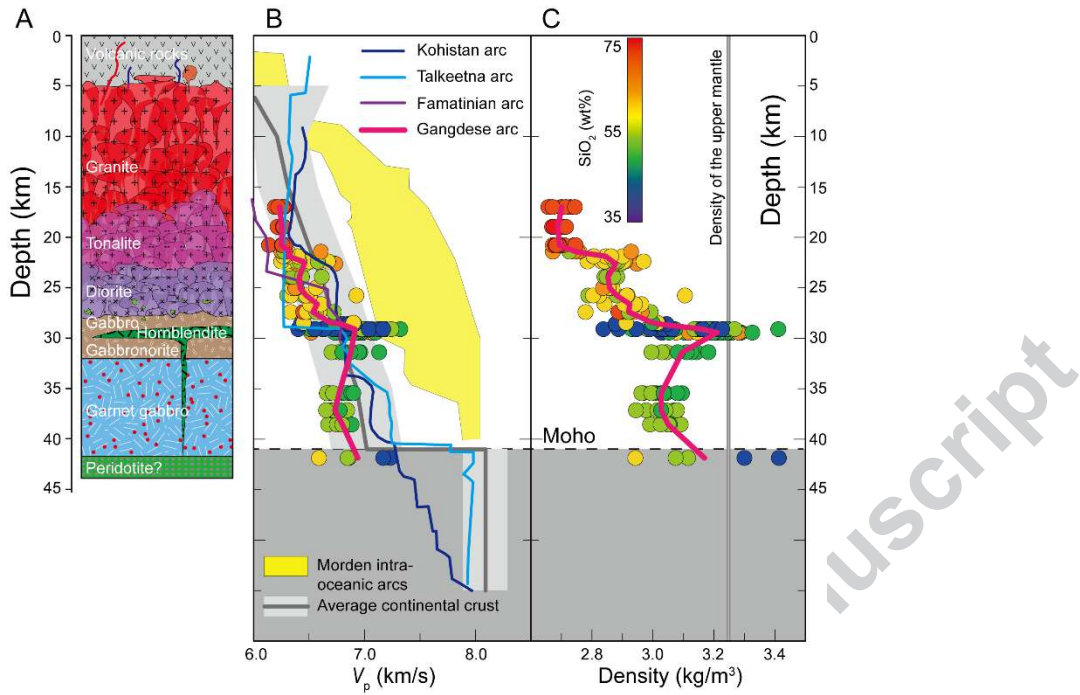


**Fig. 1** (A) Tectonic framework of the **Lhasa terrane** showing the **Gangdese arc batholith and volcanic rocks**. (B)

Geological map of the easternmost Gangdese arc showing the sample locations. The map is based on own field observation and published studies. **Published** zircon U-Pb ages are from Guan et al. (2010, 2012), Guo et al. (2012, 2013), Ji et al. (2014), Ma et al. (2013a, 2013b), Tang et al. (2019), Zhang et al. (2020), and Zhu et al. (2011). The pressure and temperature conditions of the Kanniang complex are from Zhang et al. (2010c, 2014). (C) Cross section through the Lilong Complex in the easternmost Gangdese arc showing intrusion pressures **constrained by Al-in-amphibole barometry in this study. DMSZ = Dongjiu-Miling shear zone.**

**Fig. 2** Field photographs illustrating contact relationships and typical lithologies from the Lilong Complex. (A) Contact relationship between the olivine hornblende pyroxenite and pyroxene hornblendite. (B) Gradational contact between the hornblendite and plagioclase hornblendite. (C) Magmatic layering defined by the alternation of plagioclase-poor and plagioclase-rich bands in the hornblende gabbro. (D) Foliated hornblende gabbro containing irregular hornblendite enclave. (E) Contact relationship between ultramafic (pyroxene hornblendite) and mafic-intermediate (gabbro) sequences. (F) The Wolong granite containing green epidote (Ep).

**Fig. 3** Photomicrographs of the typical lithologies from the Lilong Complex. (A) **Euhedral/subhedral olivine crystals with interstitial orthopyroxenes and amphiboles in the pyroxene hornblende peridotite.** (B) **The hornblende pyroxenite showing that subhedral clinopyroxene and orthopyroxene crystals with interstitial amphiboles.** (C) **Subhedral or anhedral clinopyroxene grains occur as inter-granular clusters or as inclusions in the amphiboles from the pyroxene hornblendite.** (D) **Plagioclase hornblendites exhibit orthocumulate texture and consist of coarse euhedral amphibole and interstitial anhedral plagioclase.** (E) **Clinopyroxene and orthopyroxene in the hornblende gabbro are rimmed by amphiboles.** (F) **Poikilitic amphibole in the hornblende gabbro contains inclusions of plagioclase, clinopyroxene, and magnetite.** (G) **Amphibole grains in the tonalite contain euhedral plagioclase,**

orthopyroxene, and magnetite. (H) Subhedral or euhedral epidote grains intimately associated with biotite, quartz, and plagioclase in the tonalite. Mineral abbreviations: amphibole = Amp; biotite = Bt; clinopyroxene = Cpx; epidote = Ep; quartz = Qtz; Magnetite = Mag; olivine = Ol; orthopyroxene = Opx.

**Fig. 4** Harker diagrams illustrating the different fractionation trends for the ultramafic and mafic-intermediate sequences from the Lilong Complex and the Wolong **granitoids**. The blue and purple solid lines refer to the trajectories of cumulate evolution for hydrous and anhydrous fractionation experiments (Müntener and Ulmer 2018), respectively. The blue and purple dash lines in (F) denote the trends of liquid evolution for the hydrous Southern Plutonic Complex and less hydrous Chilas Complex from the Kohistan arc (Jagoutz et al. 2011). **Published** data are from Guan et al. (2010), Ji et al. (2014), Ma et al. (2013a, 2013b), Tang et al. (2019), Wen et al. (2008), Yin et al. (2019), and Zhang et al. (2010b, 2014, 2020).

**Fig. 5** Primitive mantle-normalized rare earth element and trace element **spider** diagrams of the ultramafic (A and B) and mafic-intermediate (C and D) sequences from the Lilong Complex and the Wolong **granitoids** (E and F). Primitive mantle values are from McDonough and Sun (1995).

**Fig. 6** Cathodoluminescence (CL) images of representative zircons from the hornblende gabbro (A), quartz diorite (B), tonalites (C, D, and E), and hornblendites (F and G) in the Lilong Complex and the Wolong granite (H). The solid circles show LA-ICP-MS dating spots and corresponding  $^{206}\text{Pb}/^{238}\text{U}$  ages (in Ma), and the dashed circles show locations of Lu-Hf isotope analysis and corresponding  $\epsilon_{\text{Hf}}(t)$  values.

**Fig. 7** Zircon U-Pb concordia diagrams for the hornblende gabbro (A), quartz diorite (B), tonalites (C, D,

and E), and hornblendites (F and G) in the Lilong Complex and the Wolong granite (H). **Analyses excluded as discordant age outliers are dashed.**

**Fig. 8** Whole-rock initial ( $^{87}\text{Sr}/^{86}\text{Sr}$ )<sub>i</sub> versus  $\epsilon_{\text{Nd}}(t)$  (A) and zircon  $\epsilon_{\text{Hf}}(t)$  versus ages (B) diagrams for the Kanniang Complex, the Lilong Complex and the Wolong granite. **Symbols as in Fig. 4 except for pentagrams that represent the garnet gabbros from the Kanniang Complex.** The mixing curve is constructed using the Wolong granite sample T026 (Sr = 626 ppm, Nd = 18 ppm, ( $^{87}\text{Sr}/^{86}\text{Sr}$ )<sub>i</sub> = 0.70438, and  $\epsilon_{\text{Nd}}(t)$  = +3.5) from Wen et al. (2008) and the average composition of the Nyingchi gneisses (Sr = 157 ppm, Nd = 40 ppm, ( $^{87}\text{Sr}/^{86}\text{Sr}$ )<sub>i</sub> = 0.72382, and  $\epsilon_{\text{Nd}}(t)$  = -12.7) from Zhang et al. (2010a). **Published** data are from Guan et al. (2010), Guo et al. (2013), Ji et al. (2014), Ma et al. (2013a, 2013b), Yin et al. (2019), Tang et al. (2019), and Zhang et al. (2014, 2020).

**Fig. 9** Whole-rock trace-element (Ga/Yb)<sub>N</sub> versus SiO<sub>2</sub> (A), Sr/Y versus SiO<sub>2</sub> (B), and (La/Sm)<sub>N</sub> versus (Gd/Yb)<sub>N</sub> ratios (C) for the **Lilong** Complex and the Wolong granitoids from the Gangdese arc crustal section. The published data sources are same as **Fig. 4.**

**Fig. 10** Zircon U–Pb ages with  $2\sigma$  uncertainty for the **Kanniang** Complex, the Lilong Complex and the Wolong **granitoids**. The igneous emplacement age of the protolith of the garnet gabbros from the Kanniang Complex is undistinguished from the Lilong Complex within two sigma uncertainty. **Published** data sources are **the** same as **Fig. 8.**

**Fig. 11** (A and B) The variation of SiO<sub>2</sub> and MgO with time for the Wolong granitoids. (C and D) The spatial variation of whole-rock  $\epsilon_{\text{Nd}}(t)$  and initial ( $^{87}\text{Sr}/^{86}\text{Sr}$ )<sub>i</sub> for the Wolong granitoids. The black bars in (C) and (D)



represent the longitude of the 352–355 Ma granodiorites (Ji et al., 2012). Symbols as in Fig. 4.

**Fig. 12** Whole-rock Mg#, CaO, and Al<sub>2</sub>O<sub>3</sub> versus SiO<sub>2</sub> diagrams illustrating the whole-rock evolution of the ultramafic sequence in the Lilong Complex and the Wolong **granitoids** compared to the cumulates and liquids derived from hydrous (circles) and anhydrous (squares) fractional crystallization experiments (Müntener and Ulmer 2018). The hydrous (solid line) and anhydrous (dash lines) fractionation lines are shown in (C) SiO<sub>2</sub> versus Al<sub>2</sub>O<sub>3</sub> (Müntener and Ulmer 2018).

**Fig. 13** Schematic illustrations of the lithology (A), calculated seismic  $V_P$  (B) and density (C) depth-structure of the exposed Gangdese arc deep crustal section. Mineral density and seismic velocity are calculated using pressures derived from geothermobarometry of the observed mineral compositions and temperature calculated along steady-state 60 mW/m<sup>2</sup> geotherm. Comparison of calculated  $V_P$  profiles with the seismic wave velocities for the average continental crust (Christensen and Mooney, 1995), oceanic arc crust (Calvert, 2011), and calculated velocities depth-structures of the Kohistan (Jagoutz and Behn, 2013), Talkeetna (Behn and Kelemen, 2006), and Famatinian arcs (Tibaldi et al., 2013).

**Fig. 14** (A) Major and trace element concentrations of different building units of the Gangdese arc deep crust and the average Gangdese arc lower crust normalized to the lower continental crust of Rudnick and Gao (2014). (B) Major and trace element concentrations of the Gangdese arc lower crust (this study and Zhang et al. 2020), the Famatinian and the Fiordland continental arc lower crust, the Talkeetna and Kohistan oceanic arc lower crust (Jagoutz and Kelemen 2015), and the newly estimated lower continental crust (Hacker et al. 2015) normalized to the lower continental crust of Rudnick and Gao (2014). The gray field is the composition range of published lower

continental crust from Rudnick and Gao (2014). The data used to calculate the composition of Famatinian arc lower crust are from Otamendi et al. (2009a, 2009b, 2010, 2012, 2016) and Walker et al. (2015). The data used to calculate the composition of Fiordland arc lower crust are from Chapman (2017), Dunkley (2010), Watton (2009) and Wiesenfeld (2016).

Author accepted manuscript